Finite electro-elasticity with physics-augmented neural networks

Dominik K. Klein[1,*], Rogelio Ortigosa[2],
Jesús Martínez-Frutos[2], and Oliver Weeger[1]

[1] *Cyber-Physical Simulation Group & Graduate School of Computational Engineering,*
Department of Mechanical Engineering & Centre for Computational Engineering,
Technical University of Darmstadt, Dolivostr. 15, 64293 Darmstadt, Germany
[2] *Technical University of Cartagena, Campus Muralla del Mar, 30202, Cartagena (Murcia), Spain*
[*] *Corresponding author, email: klein@cps.tu-darmstadt.de*

July 30, 2022

Abstract

In the present work, a machine learning based constitutive model for electro-mechanically coupled material behavior at finite deformations is proposed. Using different sets of invariants as inputs, an internal energy density is formulated as a convex neural network. In this way, the model fulfills the polyconvexity condition which ensures material stability, as well as thermodynamic consistency, objectivity, material symmetry, and growth conditions. Depending on the considered invariants, this physics-augmented machine learning model can either be applied for compressible or nearly incompressible material behavior, as well as for arbitrary material symmetry classes. The applicability and versatility of the approach is demonstrated by calibrating it on transversely isotropic data generated with an analytical potential, as well as for the effective constitutive modeling of an analytically homogenized, transversely isotropic rank-one laminate composite and a numerically homogenized cubic metamaterial. These examinations show the excellent generalization properties that physics-augmented neural networks offer also for multi-physical material modeling such as nonlinear electro-elasticity.

Key words: nonlinear electro-elasticity, constitutive modeling, physics-augmented machine learning, electro-active polymers, homogenization

1 Introduction

Electro active polymers (EAPs) belong to a class of multi-functional materials, which can undergo significantly large electrically induced deformations when subjected to an electric field [48, 71]. They can be broadly classified into ionic EAPs, activated by transport of ions, and electronic EAPs, actuated through the application of an electric field. Dielectric elastomers (DEs) are recognised as one of the most popular electronic EAPs [72, 73] due to their outstanding actuation capabilities (i.e., light weight, fast response time, flexibility, low stiffness properties), which makes them ideal for use as soft robots [67]. However, extremely large electric fields are generally required in order

1

to access the large actuation regime in DEs, an aspect that very often places them on the risk of encountering electro-mechanical instabilities or even electrical breakdown [54, 84].

With the aim of reducing the high operational voltage required for actuation in DEs, some authors have advocated for the design of composite-based DEs [38, 39]. Typically, these composites combine an ultra-soft and low-permittivity elastomer matrix with a stiffer and high-permittivity inclusion randomly distributed in the form of fibres or particles [80, 81]. Experimental studies have demonstrated a significant enhancement in the electro-mechanical coupling performance of DE composites [38], thus reducing the operational voltage required for actuation. Multi-layered laminated DE composites have gained considerable momentum over alternative DE composites. Gei and Mutasa [28] confirmed that the actuation performance of a DE composite can be amplified with respect to that of a single-phase DE, by optimizing the contrast and volume fraction of the DE composite constituents.

For rank-one laminate composites, it is possible to apply rank-n homogenization principles and to obtain analytical formulas describing their effective material response [7]. However, depending on the complexity of the constitutive models of the different phases of the laminate, its effective response (i.e., homogenized stress and electric field) might only be available implicitly, requiring the solution of a nonlinear system of equations. For other types of composites, Shrimali, Lefevre, and Lopez-Pamies [79] have used analytical homogenization to derive explicit analytical formulas for the behavior of porous-type materials. Unfortunately, analytical expressions might not be available in general, for instance, for metamaterials such as an elastomeric matrix with a stiff spherical or ellipsoidal inclusion. In these cases, computational homogenization methods need to be applied in order to obtain the effective response of the composite. However, the use of computational homogenization methods in the context of concurrent multiscale simulations entails extremely high computational costs, as it requires the repeated solution of boundary value problems across scales [45]. Therefore, the derivation of effective constitutive models that can capture the physics of complex electro-mechanical metamaterials would entail an extraordinary benefit.

Constitutive models should generally well approximate the available data of the material response (whether coming from experiments, analytical or computational homogenization), but also comply with physical requirements, i.e., objectivity, material symmetry, etc. For instance, to comply with thermodynamic consistency requirements, constitutive models in (electro-) elasticity are typically formulated in terms of an internal energy density [19]. Furthermore, the concept of material stability can be related to the mathematical condition of ellipticity [97] or rank-one convexity of the internal energy density [53, 58]. It prevents the formation of extremely localized deformation modes, guarantees the propagation of real travelling plane waves in the material [76], and ensures the well-posedness of the underlying boundary value problem [58]. A sufficient condition complying with the ellipticity condition is the polyconvexity of the internal energy density [5, 6, 8, 75]. This concept was later extended from elasticity to the field of nonlinear electro-mechanics [29, 69, 82].

The analytical formulation of constitutive models that can capture the effective response of complex electro-active metamaterials, whilst complying with suitable mathematical requirements, is unfortunately far from trivial, and mostly restricted to certain types of composites [79]. However, we envision the use of data-driven methods, such as machine learning techniques, as an extremely adequate and effective tool that can help paving the way to circumvent the current limitations of analytically formulated material models.

Machine learning has reached the world of mechanical constitutive modeling for a while, sparking the development of a variety of models. They have in common that they reduce the *epistemic uncertainty* associated with analytical approaches, in the sense that they reduce their *model uncertainty* [40]: For analytical models, at some point an explicit choice for some functional relationship has to

be made. While some explicit choices have a strong physical motivation, such as the hyperelastic Hencky model [34, 35, 64, 65], most approaches are of a heuristic nature, e.g., the polynomial form of the hyperelastic Ogden model [66]. The reduced flexibility that often goes along with this human choice of functional relationship has no physical motivation, but purely stems from the necessity of an explicit form of the model. Data-driven approaches such as [24, 25] reduce this limitation by automatically choosing from a large class of parametrized analytical models, which significantly exceed the amount of models a human would examine. So called "data-driven mechanics" approaches completely abandon the formulation of a constitutive model and purely act on discrete stress-strain data [14, 46], thus making no assumption on the constitutive model at all. These "data-driven" methods have also been successfully applied to magnetics, where BH-curves are replaced by data [17, 26]. In this work, we focus on constitutive models which use artificial neural networks (ANNs) [1, 49]. By using them as highly flexible functions, an explicit choice of functional relationship is also bypassed.

This leads to the second characteristic of machine learning based constitutive models: their excellent *flexibility*. From the perspective of constitutive modeling, the major benefit of ANNs is their flexibility, in fact, they are universal approximators [37]. However, due to their high number of parameters and recursive definition, this goes along with a lack of traceability, which constitutive models need to some amount. In order to arrive at reliable model predictions it is important for a model to be physically sensible, i.e., to fulfill certain (mathematically formulated) physical requirements. Furthermore, augmenting ANN based models with physical requirements and mathematical structure can significantly decrease the amount of data required to generalize well [44], whereas uninformed ANNs would require a large amount of data which is often not available. Thus, while the specific formulations of ANN based constitutive models may be different, the importance of including constitutive conditions is generally accepted [44, 51].

As mentioned above, for (electro-) mechanical constitutive models these physical requirements and mathematical conditions were developed in the last decades [32, 89, 90], e.g., the second law of thermodynamics [83] and polyconvexity [5, 6]. While the conditions that a constitutive model should fulfill are well known, fulfilling all of them at the same time can be seen as "the main open problem of the theory of material behavior" (Truesdell and Noll [90, Section 20]), a problem which remains for ANN based models. To incorporate these requirements into ANN based models, here both methods known from analytical models, as well as novel methods specifically designed for ANNs are applied.

Starting with the more conventional methods, by a special choice of *input quantities*, i.e., invariants [41, 77], multiple constitutive requirements can be fulfilled at the same time. Using invariants as input quantities for feed-forward neural networks (FFNNs) [49] with scalar-valued output, highly flexible hyperelastic potentials [36] can be constructed [56, 87]. However, FFNNs are in general not convex, and thus the models proposed in [56, 87] do not fulfill the polyconvexity condition. For this, a special choice of *network architecture* is required. Using input convex neural networks (ICNNs) [2], some of the present authors were the first to propose a model which combines the flexibility of ANNs with the polyconvexity condition, see Klein et al. [47], later also implemented by [3], and followed by Tac, Costabal, and Tepole [86], who exploited special properties of neural ordinary differential equations [16]. Furthermore, ANNs can be *embedded in a modeling framework*, by using them only as a part of the overall model and using additional analytical terms, e.g., which fulfill coercivity conditions [47]. There is a variety of ANN based models which use invariants [43, 47, 56, 86, 88]. These methods are closely related to conventional constitutive modeling, in fact, the main difference is the use of ANNs instead of analytical formulations such as polynomials.

Additionally, there are also methods for augmenting ANN based models with constitutive requirements which are only possible in this novel machine learning framework. In particular, it is

possible to fulfill constitutive requirements not in a *hard* way, but to only *approximate* them. At a first glance, this may not seem desirable, but softening constitutive requirements can be seen as a way to bypass conflicts that arise in the simultaneous fulfillment of multiple constitutive conditions. This potentially yields the additional flexibility required to represent highly challenging material behavior. In [47], a model was proposed which only approximates the objectivity condition through data augmentation [55], which was necessary in order use the deformation gradient as model input and to get enough flexibility to represent the highly nonlinear behavior of soft lattice metamaterials. Also, elastic models can directly be formulated to map strain to stress [22] with the hyperelasticity condition, i.e., the existence of a potential, being approximated through a special choice of loss function [95]. In [60], an inelastic model was proposed which approximates the second law of thermodynamics with a physically motivated loss function. To close, these methods for *augmenting* or *informing* ANNs about physical requirements are not restricted to mechanical material modeling, but also find application in other fields of physics and engineering, e.g. [13, 15, 57, 63].

In the present work, an ANN based constitutive model for finite electro-elasticity is introduced. To the best of the authors' knowledge, this application of machine learning for electro-mechanically coupled constitutive models has not been studied at all yet. Extending the work of Klein et al. [47], different sets of electro-mechanically coupled invariants are used as input quantities of ICNNs, which are then used as internal energy functions. The resulting model is highly flexible and *physics-augmented*, i.e., it fulfills the material stability condition, as well as thermodynamic consistency, objectivity, material symmetry, and growth conditions. Depending on the considered invariants, the model can either be applied for compressible or nearly incomporessible material behavior, as well as for arbitrary material symmetry classes. This makes it suitable for the effective constitutive modeling of electro-active composites and metamaterials subject to large elastic deformations.

The outline of the manuscript is as follows. In Section 2, the basics of electro-elastic constitutive modeling relevant to this work are discussed, which are then applied to the proposed ANN based model in Section 3. As a first proof of concept, the model is applied to data generated with an analytical transversely isotropic potential in Section 4, where also some general properties of physics-augmented models are discussed. In Section 5, the model is applied for the effective material modeling of an analytically homogenized, transversely isotropic rank-one laminate composite. In Section 6, the model is further applied for the effective material modeling of a numerically homogenized cubic metamaterial. After the conclusion in Section 7, some additional information on the data generation is presented in the appendices.

Notation Throughout this work, tensor compositions and contractions are denoted by $(\boldsymbol{A}\,\boldsymbol{B})_{ij} = A_{ik}B_{kj}$, $\boldsymbol{a}\cdot\boldsymbol{b} = a_i b_i$, $\boldsymbol{A}:\boldsymbol{B} = A_{ij}B_{ij}$ and $(\mathbb{A}:\boldsymbol{A})_{ij} = \mathbb{A}_{ijkl}A_{kl}$, respectively, with vectors $\boldsymbol{a}$ and $\boldsymbol{b}$, second order tensors $\boldsymbol{A}$ and $\boldsymbol{B}$ and fourth order tensor $\mathbb{A}$. The tensor product is denoted by $\otimes$, the second order identity tensor by $\boldsymbol{I}$. The gradient operator is denoted by $\boldsymbol{\nabla}$ and the divergence operator by $\boldsymbol{\nabla}\cdot$. A zero as the lower index next to the nabla symbol indicates that the operation is carried out in the referential configuration. The operator $\times$ is defined as $(\boldsymbol{A}\times\boldsymbol{B})_{iI} = \mathcal{E}_{ijk}\mathcal{E}_{IJK}A_{jJ}B_{kK}$, where $\mathcal{E}_{ijk}$ symbolises the third-order permutation tensor. For tensors in index notation, lower case indices $\{i,j,k\}$ will be used to represent the spatial configuration, whereas capital case indices $\{I,J,K\}$ will be used to represent the material description. The first Fréchet derivative of a function f w.r.t. $\boldsymbol{X}$ is denoted by $\partial f/\partial\boldsymbol{X}$. The set of invertible second order tensors with positive determinant is denoted by $\mathrm{GL}^+(3) := \left\{\boldsymbol{X}\in\mathbb{R}^{3\times3}\,|\,\det\boldsymbol{X} > 0\right\}$ and the special orthogonal group in $\mathbb{R}^3$ by $\mathrm{SO}(3) := \left\{\boldsymbol{X}\in\mathbb{R}^{3\times3}\,|\,\boldsymbol{X}^T\boldsymbol{X} = \boldsymbol{I},\ \det\boldsymbol{X} = 1\right\}$. The Frobenius norm is denoted by $\|*\|$. Unimodular tensors are overlined, i.e., $\bar{\boldsymbol{A}}$ with $\det\bar{\boldsymbol{A}} = 1$.

4

2 Nonlinear continuum electro-mechanics

Let us consider the deformation of an electro-mechanically coupled continuum, such as for instance a dielectric elastomer, electro-active polymer, or metamaterial [10, 19, 61]. As shown in Fig. 1, the body is given in its reference configuration by the open domain $\mathcal{B}_0 \subset \mathbb{R}^3$ with boundary $\partial\mathcal{B}_0$ and unit outward normal $\boldsymbol{n}_0$. After the deformation, it occupies a current configuration given by the domain $\mathcal{B} \subset \mathbb{R}^3$ with boundary $\partial\mathcal{B}$ and unit outward normal $\boldsymbol{n}$. The deformation of the electro-mechanical body is defined by a mapping $\boldsymbol{\phi} : \mathcal{B}_0 \to \mathbb{R}^3$ linking material particles $\boldsymbol{X} \in \mathcal{B}_0$ to $\boldsymbol{x} = \boldsymbol{\phi}(\boldsymbol{X}) \in \mathcal{B}$. Associated with $\boldsymbol{\phi}$, the deformation gradient tensor $\boldsymbol{F} \in \mathrm{GL}^+(3)$ is defined as

$$\boldsymbol{F} = \boldsymbol{\nabla}_0 \boldsymbol{\phi}, \qquad F_{iI} = \frac{\partial \phi_i}{\partial X_I}. \tag{1}$$

Then, its determinant J and its cofactor $\boldsymbol{H}$ are defined as

$$J = \det \boldsymbol{F} = \frac{1}{6}\boldsymbol{F} : (\boldsymbol{F} \times \boldsymbol{F}), \qquad \boldsymbol{H} = \mathrm{Cof}\,\boldsymbol{F} = J\boldsymbol{F}^{-T} = \frac{1}{2}\boldsymbol{F} \times \boldsymbol{F}. \tag{2}$$

In the absence of inertia and magnetic effects, the system of partial differential equations governing the behaviour of the electro-mechanical continuum comprises the conservation of linear momentum and the compatibility equation (1), along with the quasi-static version of the Gauss' and Faraday's laws. The coupled boundary value problem can be recast in a total Lagrangian formalism as

$$\begin{cases} \boldsymbol{F} = \boldsymbol{\nabla}_0 \boldsymbol{\phi}, & \text{in } \mathcal{B}_0, \\ \boldsymbol{\nabla}_0 \boldsymbol{P} + \boldsymbol{f}_0 = \boldsymbol{0}, & \text{in } \mathcal{B}_0, \\ \boldsymbol{P}\boldsymbol{n}_0 = \boldsymbol{t}_0, & \text{on } \partial_{\boldsymbol{t}}\mathcal{B}_0, \\ \boldsymbol{\phi} = \bar{\boldsymbol{\phi}}, & \text{on } \partial_{\boldsymbol{\phi}}\mathcal{B}_0, \end{cases} \qquad \begin{cases} \boldsymbol{e}_0 = -\boldsymbol{\nabla}_0 \varphi, & \text{in } \mathcal{B}_0, \\ \boldsymbol{\nabla}_0 \cdot \boldsymbol{d}_0 - \rho_0 = 0, & \text{in } \mathcal{B}_0, \\ \boldsymbol{d}_0 \cdot \boldsymbol{n}_0 = -\omega_0, & \text{on } \partial_{\omega}\mathcal{B}_0, \\ \varphi = \bar{\varphi}, & \text{on } \partial_{\varphi}\mathcal{B}_0, \end{cases} \tag{3}$$

where $\boldsymbol{f}_0$ represents a body force per unit undeformed volume $\mathcal{B}_0$, $\boldsymbol{t}_0$, the traction force per unit undeformed area on $\partial_{\boldsymbol{t}}\mathcal{B}_0 \subset \partial\mathcal{B}_0$, $\bar{\boldsymbol{\phi}}$, the value of the Dirichlet boundary condition on $\partial_{\boldsymbol{\phi}}\mathcal{B}_0 \subset \partial\mathcal{B}_0$, with $\partial_{\boldsymbol{t}}\mathcal{B}_0 \cup \partial_{\boldsymbol{\phi}}\mathcal{B}_0 = \partial\mathcal{B}_0$ and $\partial_{\boldsymbol{t}}\mathcal{B}_0 \cap \partial_{\boldsymbol{\phi}}\mathcal{B}_0 = \emptyset$. Furthermore, ρ_0 represents an electric volume charge per unit of undeformed volume $\mathcal{B}_0$, and ω_0 an electric surface charge per unit of undeformed area $\partial_{\omega}\mathcal{B}_0 \subset \partial\mathcal{B}_0$. In addition, $\boldsymbol{e}_0$ is the Lagrangian electric field vector, $\varphi : \mathcal{B}_0 \to \mathbb{R}$, the scalar electric potential, and $\partial_{\varphi}\mathcal{B}_0$, the part of the boundary $\partial\mathcal{B}_0$ where essential electric potential boundary conditions are applied so that $\partial_{\omega}\mathcal{B}_0 \cup \partial_{\varphi}\mathcal{B}_0 = \partial\mathcal{B}_0$ and $\partial_{\omega}\mathcal{B}_0 \cap \partial_{\varphi}\mathcal{B}_0 = \emptyset$. Finally, $\boldsymbol{P}$ and $\boldsymbol{d}_0$ represent the first Piola-Kirchhoff stress tensor and the Lagrangian electric displacement field, respectively.

2.1 Constitutive equations of electro-elasticity

In reversible nonlinear electro-mechanics, i.e., finite deformation electro-elasticity, the constitutive relationships required for the closure of Eq. (3) can be defined in terms of the internal energy e per unit undeformed volume $\mathcal{B}_0$ [29, 69]. This energy potential depends solely on the deformation gradient tensor $\boldsymbol{F}$ and on the material electric displacement field $\boldsymbol{d}_0$, namely

$$e : \mathrm{GL}^+(3) \times \mathbb{R}^3 \to \mathbb{R}, \qquad (\boldsymbol{F}, \boldsymbol{d}_0) \mapsto e(\boldsymbol{F}, \boldsymbol{d}_0). \tag{4}$$

For simplicity, we write $e = e(\boldsymbol{\mathcal{U}})$ with $\boldsymbol{\mathcal{U}} = \{\boldsymbol{F}, \boldsymbol{d}_0\}$. Differentiation of the internal energy with respect to its arguments yields the first Piola-Kirchhoff stress tensor and the material electric field as

$$\boldsymbol{P}(\boldsymbol{\mathcal{U}}) = \frac{\partial e(\boldsymbol{\mathcal{U}})}{\partial \boldsymbol{F}}, \qquad \boldsymbol{e}_0(\boldsymbol{\mathcal{U}}) = \frac{\partial e(\boldsymbol{\mathcal{U}})}{\partial \boldsymbol{d}_0}. \tag{5}$$
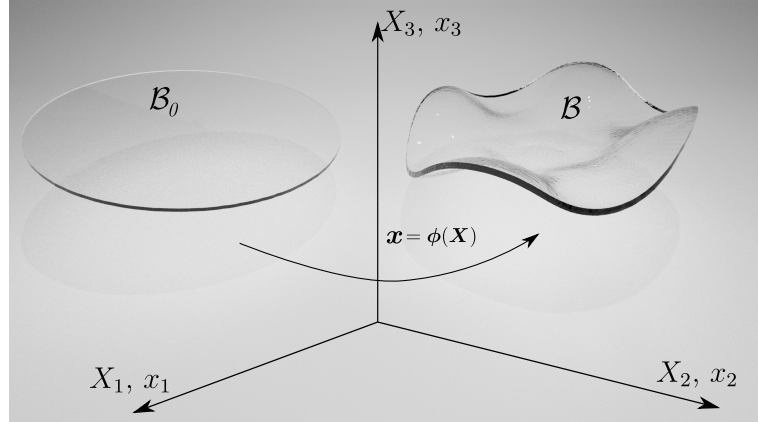
Figure 1: Deformation of the body in the reference configuration $\mathcal{B}_0$ of an electro-mechanically coupled continuum can be induced with an electric field, leading to the deformed configuration $\mathcal{B}$. Figure taken from [70].

Following the work of [29, 69], where an extension of the concept of polyconvexity [5, 6] was proposed into the field of nonlinear electro-mechanics, we consider internal energies which are polyconvex. Thus, e can be written as

$$e\left(\boldsymbol{\mathcal{U}}\right) = \mathcal{P}\left(\boldsymbol{\mathcal{V}}\right), \qquad \boldsymbol{\mathcal{V}} = (\boldsymbol{F}, \boldsymbol{H}, J, \boldsymbol{d}_0, \boldsymbol{d}) \in \mathbb{R}^{25}, \tag{6}$$

where the spatial vector field $\boldsymbol{d}$ is defined as $\boldsymbol{d} = \boldsymbol{F}\boldsymbol{d}_0$ and $\mathcal{P}$ is a convex function with respect to its 25 arguments.

Remark 2.1. Notice that the fifth argument in the definition of the polyconvex internal energy in Eq. (6), namely the vector field $\boldsymbol{d}$, must not be confused with the spatial or Eulerian counterpart of the material electric displacement field $\boldsymbol{d}_0$, here denoted as $\boldsymbol{d}^*$. The relationship between $\boldsymbol{d}_0$ and $\boldsymbol{d}^*$ can be obtained through the standard Piola transformation $\boldsymbol{d}_0 = \boldsymbol{H}^T\boldsymbol{d}^*$, i.e., $\boldsymbol{d}^* = J^{-1}\boldsymbol{d}$. Furthermore, the Eulerian material electric field $\boldsymbol{e}_0$ is related to its spatial counterpart $\boldsymbol{e}^*$ through the push-forward transformation $\boldsymbol{e}_0 = \boldsymbol{F}^T\boldsymbol{e}^*$.

In addition to the electric displacement field and the electric field, it is customary to introduce the polarization vector, which is defined in the material setting according to

$$\boldsymbol{p}_0 = \boldsymbol{d}_0 - \varepsilon_0 J \boldsymbol{C}^{-1}\boldsymbol{e}_0, \qquad \boldsymbol{C} = \boldsymbol{F}^T\boldsymbol{F}, \tag{7}$$

with ε_0 being the electric permittivity of vacuum. The push-forward relationship relating the material polarization vector field $\boldsymbol{p}_0$ to its spatial counterpart $\boldsymbol{p}^*$ is $\boldsymbol{p}_0 = \boldsymbol{H}^T\boldsymbol{p}^*$.

For sufficiently differentiable functions $\mathcal{P}$, the polyconvexity condition can be formulated in terms of the Hessian of $\mathcal{P}$, namely

$$\delta\boldsymbol{\mathcal{V}} : \frac{\partial^2\mathcal{P}}{\partial\boldsymbol{\mathcal{V}}\partial\boldsymbol{\mathcal{V}}} : \delta\boldsymbol{\mathcal{V}} \geq 0 \quad \forall \delta\boldsymbol{\mathcal{V}} \in \mathbb{R}^{25}, \tag{8}$$

where all the components of the (symmetric) Hessian operator $\frac{\partial^2\mathcal{P}}{\partial\boldsymbol{\mathcal{V}}\partial\boldsymbol{\mathcal{V}}}$ are given as

$$\frac{\partial^2\mathcal{P}}{\partial\boldsymbol{\mathcal{V}}\partial\boldsymbol{\mathcal{V}}} = \begin{bmatrix} \frac{\partial^2\mathcal{P}}{\partial\boldsymbol{F}\partial\boldsymbol{F}} & \frac{\partial^2\mathcal{P}}{\partial\boldsymbol{F}\partial\boldsymbol{H}} & \frac{\partial^2\mathcal{P}}{\partial\boldsymbol{F}\partial J} & \frac{\partial^2\mathcal{P}}{\partial\boldsymbol{F}\partial\boldsymbol{d}_0} & \frac{\partial^2\mathcal{P}}{\partial\boldsymbol{F}\partial\boldsymbol{d}} \\ & \frac{\partial^2\mathcal{P}}{\partial\boldsymbol{H}\partial\boldsymbol{H}} & \frac{\partial^2\mathcal{P}}{\partial\boldsymbol{H}\partial J} & \frac{\partial^2\mathcal{P}}{\partial\boldsymbol{H}\partial\boldsymbol{d}_0} & \frac{\partial^2\mathcal{P}}{\partial\boldsymbol{H}\partial\boldsymbol{d}} \\ & & \frac{\partial^2\mathcal{P}}{\partial J\partial J} & \frac{\partial^2\mathcal{P}}{\partial J\partial\boldsymbol{d}_0} & \frac{\partial^2\mathcal{P}}{\partial J\partial\boldsymbol{d}} \\ & \text{symm.} & & \frac{\partial^2\mathcal{P}}{\partial\boldsymbol{d}_0\partial\boldsymbol{d}_0} & \frac{\partial^2\mathcal{P}}{\partial\boldsymbol{d}_0\partial\boldsymbol{d}} \\ & & & & \frac{\partial^2\mathcal{P}}{\partial\boldsymbol{d}\partial\boldsymbol{d}} \end{bmatrix}. \tag{9}$$

6

The polyconvexity condition is sufficient to entail the rank-one convexity or ellipticity condition, which for energies with second order differentiability can be written as

$$\delta \boldsymbol{\mathcal{U}} : \frac{\partial^2 e(\boldsymbol{\mathcal{U}})}{\partial \boldsymbol{\mathcal{U}} \partial \boldsymbol{\mathcal{U}}} : \delta \boldsymbol{\mathcal{U}} \geq 0, \qquad \forall \, \delta \boldsymbol{\mathcal{U}} = \{\boldsymbol{u} \otimes \boldsymbol{V}, \boldsymbol{V}_\perp\}, \qquad \boldsymbol{V}_\perp \cdot \boldsymbol{V} = 0, \tag{10}$$

with

$$\frac{\partial^2 e}{\partial \boldsymbol{\mathcal{U}} \partial \boldsymbol{\mathcal{U}}} = \begin{bmatrix} \frac{\partial^2 \mathcal{P}}{\partial \boldsymbol{F} \partial \boldsymbol{F}} & \frac{\partial^2 \mathcal{P}}{\partial \boldsymbol{F} \partial \boldsymbol{d}_0} \\ \frac{\partial^2 \mathcal{P}}{\partial \boldsymbol{d}_0 \partial \boldsymbol{F}} & \frac{\partial^2 \mathcal{P}}{\partial \boldsymbol{d}_0 \partial \boldsymbol{d}_0} \end{bmatrix}. \tag{11}$$

When written as in Eq. (11), the rank-one condition can be referred to as the ellipticity or Legendre-Hadamard condition, which guarantees the propagation of real travelling plane waves in the material, and the well-posedness of the boundary value problem defined in Eq. (3) [58, 76].

From the perspective of constitutive modeling, ellipticity is desired rather than polyconvexity, as ellipticity ensures a favorable numerical behavior of the model. Polyconvexity, on the other side, stems from a more theoretical context, e.g., its associated coercivity conditions make assumptions on the model behavior far outside a practically relevant deformation range [50]. However, polyconvexity is more straightforward to include in the model formulation than the ellipticity condition, and is therefore used in the present work, c.f. [47].

Remark 2.2. Polyconvexity in the sense of Eq. (6) permits to conclude that $e(\boldsymbol{\mathcal{U}}) = \mathcal{P}(\boldsymbol{\mathcal{V}})$ is in fact convex with respect to $\boldsymbol{d}_0$, namely

$$\delta \boldsymbol{d}_0 \cdot \frac{\partial^2 e(\boldsymbol{\mathcal{U}})}{\partial \boldsymbol{d}_0 \partial \boldsymbol{d}_0} \cdot \delta \boldsymbol{d}_0 \geq 0, \qquad \forall \, \delta \boldsymbol{d}_0 \in \mathbb{R}^3. \tag{12}$$

This in turn guarantees the existence of the total or amended free energy density

$$\Psi : \mathrm{GL}^+(3) \times \mathbb{R}^3 \to \mathbb{R}, \qquad (\boldsymbol{F}, \boldsymbol{e}_0) \mapsto \Psi(\boldsymbol{F}, \boldsymbol{e}_0). \tag{13}$$

For simplicity, we write $\Psi = \Psi(\boldsymbol{\mathcal{W}})$, with $\boldsymbol{\mathcal{W}} = \{\boldsymbol{F}, \boldsymbol{e}_0\}$, where Ψ is related to the polyconvex internal energy density $e(\boldsymbol{\mathcal{U}})$ by means of the Legendre transformation

$$\Psi(\boldsymbol{\mathcal{W}}) = -\sup_{\boldsymbol{d}_0} \left\{ \boldsymbol{e}_0 \cdot \boldsymbol{d}_0 - e(\boldsymbol{\mathcal{U}}) \right\}. \tag{14}$$

Remark 2.3. The internal energy density $e(\boldsymbol{F}, \boldsymbol{d}_0)$ can be additively decomposed into a polarization term and a Maxwell term [9, 11, 18, 93, 94] according to

$$e(\boldsymbol{F}, \boldsymbol{d}_0) = e_P(\boldsymbol{F}, \boldsymbol{d}_0) + e_M(\boldsymbol{F}, \boldsymbol{d}_0),$$

where the Maxwell term, when the material is immersed in vacuum, is given by

$$e_M(\boldsymbol{F}, \boldsymbol{d}_0) = \frac{1}{2J\varepsilon_0} \|\boldsymbol{d}\|^2.$$

However, according to Eq. (5), the constitutive equations relating $\{\boldsymbol{F}, \boldsymbol{e}_0\}$ and $\{\boldsymbol{P}, \boldsymbol{d}_0\}$ need to be given in terms of the total or amended energy representation $e(\boldsymbol{F}, \boldsymbol{d}_0)$. Furthermore, the requirement of polyconvexity is imposed on the total or amended internal energy density $e(\boldsymbol{F}, \boldsymbol{d}_0)$.

2.2 Invariant representation of the internal energy density

The internal energy density $e(\mathcal{U})$ must obey to the principle of objectivity or material frame indifference [90], i.e., invariance with respect to rotations $\boldsymbol{Q} \in \mathrm{SO}(3)$ in the spatial configuration, which can be formulated as

$$e\left(\boldsymbol{Q}\,\boldsymbol{F},\,\boldsymbol{d}_0\right) = e\left(\boldsymbol{F},\boldsymbol{d}_0\right) \quad \forall\,\boldsymbol{F} \in \mathrm{GL}^+(3),\,\boldsymbol{d}_0 \in \mathbb{R}^3,\,\boldsymbol{Q} \in \mathrm{SO}(3)\,. \tag{15}$$

Notice in above Eq. (15) that only the deformation gradient tensor $\boldsymbol{F}$ is multiplied by arbitrary rotations $\boldsymbol{Q}$, as this is a two-point tensor, and hence, lying in both spatial and material configurations. This is not the case for the material electric field $\boldsymbol{d}_0$, which is solely related to the reference or material configuration, and hence, already implying objectivity.

In addition, the strain energy density must take into account the underlying features of the material symmetry group $\mathcal{G} \subseteq O(3)$ characterizing the isotropic or anisotropic behaviour of the material. The material symmetry condition [31] can be represented as

$$e(\boldsymbol{F}\,\boldsymbol{Q},\,\boldsymbol{Q}\,\boldsymbol{d}_0) = e(\boldsymbol{F},\boldsymbol{d}_0) \quad \forall\,\boldsymbol{F} \in \mathrm{GL}^+(3),\,\boldsymbol{d}_0 \in \mathbb{R}^3,\,\boldsymbol{Q} \in \mathcal{G} \subseteq O(3)\,. \tag{16}$$

Making use of the concept of structural tensors, and representation theorems of tensor functions, the authors in [21, 75, 78] considered second order structural tensors $\boldsymbol{G}^{\mathcal{G}}$ and fourth order structural tensors $\mathbb{G}^{\mathcal{G}}$ to characterize an underlying material symmetry group $\mathcal{G} \subseteq O(3)$, hence, satisfying the following invariance relations with respect to transformations $\boldsymbol{Q} \in \mathcal{G} \subseteq O(3)$, namely

$$\left. \begin{aligned} \boldsymbol{Q}\boldsymbol{G}^{\mathcal{G}}\boldsymbol{Q}^T &= \boldsymbol{G}_{\mathcal{G}} \\ \boldsymbol{Q} \boxtimes \boldsymbol{Q} : \mathbb{G}^{\mathcal{G}} : \boldsymbol{Q}^T \boxtimes \boldsymbol{Q}^T &= \mathbb{G}^{\mathcal{G}} \end{aligned} \right\} \quad \forall\,\boldsymbol{Q} \in \mathcal{G} \subseteq O(3)\,, \tag{17}$$

with

$$\left(\boldsymbol{Q} \boxtimes \boldsymbol{Q} : \mathbb{G}^{\mathcal{G}} : \boldsymbol{Q}^T \boxtimes \boldsymbol{Q}^T \right)_{IJKL} = Q_{IR}Q_{JS}Q_{KT}Q_{LU} \left(\mathbb{G}^{\mathcal{G}} \right)_{RSTU}\,. \tag{18}$$

By making use of the isotropicisation theorem [98], strain energy density functions complying with the material symmetry condition can be defined [21] by re-expressing the anisotropic restriction (16) for every $\boldsymbol{Q} \in O(3)$ as

$$e^{\mathcal{G}}(\boldsymbol{F}\boldsymbol{Q},\boldsymbol{Q}\boldsymbol{d}_0,\boldsymbol{Q}\boldsymbol{G}^{\mathcal{G}}\boldsymbol{Q}^T,\boldsymbol{Q} \boxtimes \boldsymbol{Q} : \mathbb{G}^{\mathcal{G}} : \boldsymbol{Q}^T \boxtimes \boldsymbol{Q}^T) = e^{\mathcal{G}}(\boldsymbol{F},\boldsymbol{d}_0,\boldsymbol{Q}^{\mathcal{G}},\mathbb{G}^{\mathcal{G}})\,. \tag{19}$$

In addition to the objectivity and material symmetry conditions in Eqs. (15) and (16), respectively, the internal energy must comply with the following conditions

$$e\left(\mathcal{U}\right)|_{\boldsymbol{F}=\boldsymbol{I},\boldsymbol{d}_0=\boldsymbol{0}} = 0\,, \qquad \left.\frac{\partial e\left(\mathcal{U}\right)}{\partial \boldsymbol{F}}\right|_{\boldsymbol{F}=\boldsymbol{I},\boldsymbol{d}_0=\boldsymbol{0}} = \boldsymbol{0}\,, \qquad \left.\frac{\partial e\left(\mathcal{U}\right)}{\partial \boldsymbol{d}_0}\right|_{\boldsymbol{F}=\boldsymbol{I},\boldsymbol{d}_0=\boldsymbol{0}} = \boldsymbol{0}\,, \tag{20}$$

which essentially entail that the internal energy, the first Piola-Kirchhoff stress tensor, and the material electric field must vanish in the origin, i.e., for $\boldsymbol{F} = \boldsymbol{I}$ and $\boldsymbol{d}_0 = \boldsymbol{0}$.

By formulating constitutive models in terms of invariants [41], they can fulfill both the material symmetry and objectivity condition by construction. To ensure polyconvexity, see Eq. (8), it is important to use invariants which are convex in $\boldsymbol{\mathcal{V}}$, see Eq. (6). Furthermore, the compressibility properties of a material must be considered, i.e., if it is compressible or nearly incompressible. In the compressible case, the growth condition $e(\mathcal{U}) \to \infty$ as $J \to 0^+$ must be fulfilled, while for nearly incompressible materials $J \approx 1$ must hold. In order to fulfill these conditions, an additional volumetric term $\mathcal{P}_{\mathrm{vol}}(J)$ is added to the internal energy. Overall, the internal energy, c.f. Eq. (6), can be expressed as

$$e(\mathcal{U}) = \mathcal{P}(\boldsymbol{\mathcal{V}}) = \widetilde{\mathcal{P}}(\boldsymbol{\mathcal{I}}) + \mathcal{P}_{\mathrm{vol}}(J)\,. \tag{21}$$

where $\boldsymbol{\mathcal{I}} : \boldsymbol{\mathcal{V}} \to \mathbb{R}^n$ are invariants of the symmetry group under consideration and $\mathcal{P}_{\text{vol}}(J)$ is chosen according to the compressible or nearly incompressible nature of the material under consideration. The growth condition for compressible materials can be fulfilled by the term

$$\mathcal{P}_{\text{vol}}(J) = \alpha \left(J + \frac{1}{J} - 2 \right)^2 , \tag{22}$$

while the condition $J \approx 1$ for nearly incompressible materials can be fulfilled by the term

$$\mathcal{P}_{\text{vol}}(J) = \alpha \, (J - 1)^2 . \tag{23}$$

In both cases, $\mathcal{P}_{\text{vol}}(J)$ is convex w.r.t. J and thus polyconvex, and $\alpha > 0$ is a (possibly large) penalty parameter with units of stress. We now introduce invariants for all symmetry groups considered in the present work. For a detailed description of the symmetry groups see Zheng [98].

2.2.1 Isotropic electro-mechanics

For nearly incompressible materials, invariants can either be formulated in the full deformation gradient $\boldsymbol{F}$ or in its isochoric part $\bar{\boldsymbol{F}} = J^{-1/3} \boldsymbol{F}$. The latter is motivated from the purely mechanical, nearly incompressible, isotropic case. For this special case, which can describe a wide range of elastomeric materials, the two isochoric invariants

$$\bar{I}_1 = J^{-2/3} \|\boldsymbol{F}\|^2 , \qquad \bar{I}_2 = J^{-2} \|\boldsymbol{H}\|^3 , \tag{24}$$

can be constructed. Note that while $\bar{I}_1$ is polyconvex, the typically employed isochoric invariant $\bar{I}_2^* = J^{-4/3} \|\boldsymbol{H}\|^2$ is not. Thus, we here use the slightly adapted invariant $\bar{I}_2 = (\bar{I}_2^*)^{3/2}$, which is again polyconvex [30]. Setting $\boldsymbol{\mathcal{I}} = \{\bar{I}_1, \bar{I}_2\}$ in Eq. (21), the multiplicative decomposition of the deformation gradient and the additive split of the internal energy have two implications: first of all, isochoric deformations will only produce a deviatoric Cauchy stress, which represents a physically sensible behavior for isotropic bodies, c.f. Sansour [74]. Furthermore, this correspondence between isochoric deformation and deviatoric stress is convenient for numerical applications, c.f. Wriggers [96, Section 10.1].

However, when anisotropy or electrical effects are considered, this correspondence is not a physically sensible assumption anymore [74]. Beside that, even when constructing the invariants for this case with the isochoric part of the deformation gradient, this stress correspondence would not hold anymore. Therefore, both the anisotropic and mixed invariants are constructed with the full deformation gradient also for the nearly incompressible case, while the isotropic, isochoric invariants are constructed with the isochoric part of the deformation gradient for the nearly incompressible case. Hence, the following two possibilities are considered for the internal energy in the additive decomposition in Eq. (21)

$$\widetilde{\mathcal{P}} = \widetilde{\mathcal{P}}(\boldsymbol{\mathcal{I}}) : \mathbb{R}^5 \to \mathbb{R} \quad \text{with} \quad \boldsymbol{\mathcal{I}} = \begin{cases} \boldsymbol{\mathcal{I}}^{\text{iso}} = \{I_1, I_2, I_4, I_5, J\} , & \text{(Compressible case)} \\ \bar{\boldsymbol{\mathcal{I}}}^{\text{iso}} = \{\bar{I}_1, \bar{I}_2, I_4, I_5, J\} , & \text{(Nearly incompressible case)} \end{cases} , \tag{25}$$

with the further invariants

$$I_1 = \|\boldsymbol{F}\|^2 , \qquad I_2 = \|\boldsymbol{H}\|^2 , \qquad I_4 = \|\boldsymbol{d}_0\|^2 , \qquad I_5 = \|\boldsymbol{d}\|^2 . \tag{26}$$

Proof of convexity of all the mechanical invariants featuring in (26) can be found in [30, 78]. Note that, even for $J \approx 1$, it is important to include J, which becomes clear when considering standard representation theorems [41].

Remark 2.4. An additional invariant, which completes the integrity basis of isotropic electro-elasticity, is the following

$$I_6 = \|\boldsymbol{H}\boldsymbol{d}_0\|^2 . \tag{27}$$

However, above invariant is not polyconvex, as the condition specified in Eq. (8) is not satisfied, namely

$$\delta\boldsymbol{\mathcal{V}} : \frac{\partial^2 I_6}{\partial\boldsymbol{\mathcal{V}}\partial\boldsymbol{\mathcal{V}}} : \delta\boldsymbol{\mathcal{V}} = 2\|\delta\boldsymbol{H}\,\boldsymbol{d}_0 + \boldsymbol{H}\,\delta\boldsymbol{d}_0\|^2 + 4(\delta\boldsymbol{H}\,\delta\boldsymbol{d}_0)\cdot(\boldsymbol{H}\,\boldsymbol{d}_0), \tag{28}$$

Taking $\delta\boldsymbol{H} = \boldsymbol{H}$ and $\delta\boldsymbol{d}_0 = -\boldsymbol{d}_0$ yields

$$\delta\boldsymbol{\mathcal{V}} : \frac{\partial^2 I_6}{\partial\boldsymbol{\mathcal{V}}\partial\boldsymbol{\mathcal{V}}} : \delta\boldsymbol{\mathcal{V}} = -4\|\boldsymbol{H}\,\boldsymbol{d}_0\|^2, \tag{29}$$

which is clearly negative and hence, non-convex with respect to the elements of the set $\boldsymbol{\mathcal{V}}$. Therefore, I_6 is not included in the list of polyconvex invariants as specified in Eq. (25).

Notice however, that, as shown in [29], it would be possible to include a polyconvex version of the invariant I_6. This can be achieved through the following "polyconvexification" technique, which entails the definition of the overall polyconvex invariant I_6^*, as

$$I_6^* = \alpha^2 I_2^2 + \beta^2 I_4^2 + 2\alpha\beta I_6, \qquad \text{with} \quad \alpha, \beta > 0. \tag{30}$$

I_6^* satisfies that the following Hessian operator

$$\begin{bmatrix} \frac{\partial^2 I_6^*}{\partial\boldsymbol{H}\partial\boldsymbol{H}} & \frac{\partial^2 I_6^*}{\partial\boldsymbol{H}\partial\boldsymbol{d}_0} \\ \frac{\partial^2 I_6^*}{\partial\boldsymbol{d}_0\partial\boldsymbol{H}} & \frac{\partial^2 I_6^*}{\partial\boldsymbol{d}_0\partial\boldsymbol{d}_0} \end{bmatrix} \tag{31}$$

is positive definite $\forall\boldsymbol{H},\boldsymbol{d}_0$.

As it can be observed in Sections 4 to 6, in this work we are able to obtain reasonably accurate approximations of complex constitutive behaviors using an incomplete set of polyconvex invariants for the formulation of the internal energy density $e(\boldsymbol{F},\boldsymbol{d}_0)$. Thus, our preference is to advocate for simplicity whenever permitted, restricting to the current incomplete but polyconvex set of invariants, rather than including the additional, sophisticated polyconvexified invariant.

Only when the invariant-based formulation presented in Section 3 might not be sufficient to accurately reproduce data, alternative approaches might be needed. For instance, in [47], an approach where the inputs of the neural network are the components of the deformation gradient tensor itself instead of invariants, is also presented. In this approach, however, the satisfaction of material frame indifference needs to be "learned" by the neural network (i.e., it cannot be satisfied a priori), in contrast to the current invariant-based formulation. Comparing both invariant-based and deformation gradient-based approaches in electro-mechanics will be a subject of future work.

2.2.2 Transversely isotropic material symmetry

A single second order structural tensor $\boldsymbol{G}^{\text{ti}}$ suffices to characterise the material symmetry group $\mathcal{D}_{\infty h}$ of transverse isotropy [20, 99, 100]. Assuming a preferred (unitary) direction $\boldsymbol{n}$ in the reference configuration, it is defined as

$$\boldsymbol{G}^{\text{ti}} = \boldsymbol{n}\otimes\boldsymbol{n}. \tag{32}$$

In addition to the isotropic invariants $\boldsymbol{\mathcal{I}}^{\text{iso}}$ from Eq. (26), using $\boldsymbol{G}^{\text{ti}}$, for this material symmetry group the polyconvex invariants

$$\boldsymbol{\mathcal{J}}^{\text{ti}} = \left\{ J_1^{\text{ti}}, J_2^{\text{ti}}, J_3^{\text{ti}} \right\}$$

$$\text{with} \quad J_1^{\text{ti}} = \left\|\boldsymbol{F}\,\boldsymbol{G}^{\text{ti}}\right\|^2, \qquad J_2^{\text{ti}} = \left\|\boldsymbol{H}\,\boldsymbol{G}^{\text{ti}}\right\|^2, \qquad J_3^{\text{ti}} = \text{tr}\left((\boldsymbol{d}_0\otimes\boldsymbol{d}_0)\,\boldsymbol{G}^{\text{ti}}\right), \tag{33}$$

10

can be defined, which comply with the objectivity and material symmetry conditions, c.f. Eqs. (15) and (19), respectively. Therefore, the internal energy in the additive decomposition in Eq. (21) is defined for this particular material symmetry group as

$$\widetilde{\mathcal{P}} = \widetilde{\mathcal{P}}(\boldsymbol{\mathcal{I}}) : \mathbb{R}^9 \to \mathbb{R} \quad \text{with} \quad \boldsymbol{\mathcal{I}} = \begin{cases} \left\{ \boldsymbol{\mathcal{I}}^{\text{iso}}, \boldsymbol{\mathcal{J}}^{\text{ti}} \right\}, & \text{(Compressible case)} \\ \left\{ \bar{\boldsymbol{\mathcal{I}}}^{\text{iso}}, \boldsymbol{\mathcal{J}}^{\text{ti}} \right\}, & \text{(Nearly incompressible case)} \end{cases} . \tag{34}$$

2.2.3 Cubic material symmetry

For the cubic material symmetry group $\mathcal{O}_h$, a single fourth order structural tensor $\mathbb{G}^{\text{cub}}$ suffices to characterise the underlying material symmetry attributes. It is defined as [78]

$$\mathbb{G}^{\text{cub}} = \sum_{i=1}^{3} \boldsymbol{a}_i \otimes \boldsymbol{a}_i \otimes \boldsymbol{a}_i \otimes \boldsymbol{a}_i . \tag{35}$$

Therefore, in addition to the isotropic invariants $\boldsymbol{\mathcal{I}}^{\text{iso}}$ from Eq. (26), using $\mathbb{G}^{\text{cub}}$, for the cubic material symmetry group the polyconvex invariants

$$\boldsymbol{\mathcal{J}}^{\text{cub}} = \left\{ J_1^{\text{cub}}, J_2^{\text{cub}}, J_3^{\text{cub}} \right\}$$
$$\text{with} \quad J_1^{\text{cub}} = \boldsymbol{F}^T \boldsymbol{F} : \mathbb{G}^{\text{cub}} : \boldsymbol{F}^T \boldsymbol{F} , \qquad J_2^{\text{cub}} = \boldsymbol{H}^T \boldsymbol{H} : \mathbb{G}^{\text{cub}} : \boldsymbol{H}^T \boldsymbol{H} , \tag{36}$$
$$J_3^{\text{cub}} = \boldsymbol{d}_0 \otimes \boldsymbol{d}_0 : \mathbb{G}^{\text{cub}} : \boldsymbol{I} ,$$

can be defined [20, Section 3.7], which comply with the objectivity and material symmetry conditions, c.f. Eqs. (15) and (19), respectively. Therefore, the internal energy in the additive decomposition in Eq. (21) is defined for this particular material symmetry group as

$$\widetilde{\mathcal{P}} = \widetilde{\mathcal{P}}(\boldsymbol{\mathcal{I}}) : \mathbb{R}^8 \to \mathbb{R} \quad \text{with} \quad \boldsymbol{\mathcal{I}} = \begin{cases} \left\{ \boldsymbol{\mathcal{I}}^{\text{iso}}, \boldsymbol{\mathcal{J}}^{\text{cub}} \right\}, & \text{(Compressible case)} \\ \left\{ \bar{\boldsymbol{\mathcal{I}}}^{\text{iso}}, \boldsymbol{\mathcal{J}}^{\text{cub}} \right\}, & \text{(Nearly incompressible case)} \end{cases} . \tag{37}$$

Remark 2.5. Using the fourth order cubic structural tensor from Eq. (35), an additional invariant can be constructed as

$$J_4^{\text{cub}} = \boldsymbol{d}_0 \otimes \boldsymbol{d}_0 : \mathbb{G}^{\text{cub}} : \boldsymbol{F}^T \boldsymbol{F} . \tag{38}$$

However, this invariant is not polyconvex, as Eq. (8) is not satisfied, namely

$$\delta \boldsymbol{\mathcal{V}} : \frac{\partial^2 J_4^{\text{cub}}}{\partial \boldsymbol{\mathcal{V}} \partial \boldsymbol{\mathcal{V}}} : \delta \boldsymbol{\mathcal{V}} = 2 \| \boldsymbol{u} + \boldsymbol{v} \|^2 + 4 \boldsymbol{u} \cdot \boldsymbol{v} \tag{39}$$

with $\boldsymbol{u} = \sum_{i=1}^{3} (\delta \boldsymbol{d}_0 \cdot \boldsymbol{a}_i) \boldsymbol{F} \boldsymbol{a}_i$ and $\boldsymbol{v} = \sum_{i=1}^{3} (\boldsymbol{d}_0 \cdot \boldsymbol{a}_i) \delta \boldsymbol{F} \boldsymbol{a}_i$. Taking $\boldsymbol{v} = -\boldsymbol{u}$, i.e., e.g. $\delta \boldsymbol{d}_0 = -\boldsymbol{d}_0$ and $\delta \boldsymbol{F} = \boldsymbol{F}$, yields

$$\delta \boldsymbol{\mathcal{U}} : \frac{\partial^2 J_4^{\text{cub}}}{\partial \boldsymbol{\mathcal{U}} \partial \boldsymbol{\mathcal{U}}} : \delta \boldsymbol{\mathcal{U}} = -4 \| \boldsymbol{u} \|^2 , \tag{40}$$

which is clearly negative and hence, non convex with respect to the elements of the set $\boldsymbol{\mathcal{V}}$. Therefore, J_4^{cub} is not included in the list of polyconvex invariants as specified in Eq. (36).

3 Physics-augmented neural network constitutive model

In the previous section, we discussed the form of the internal energy for compressible and nearly incompressible material behavior, c.f. Eq. (21), both formulated in terms of electro-mechanically coupled invariants. In both cases, the internal energy $e(\mathcal{U})$ comprises the polyconvex term $\widetilde{\mathcal{P}}(\mathcal{V})$, which models the behavior of the specific material, and an additional analytical term $\mathcal{P}_{\mathrm{vol}}(J)$, which ensures the desired volumetric behavior. The volumetric term can easily be analytically defined as in Eqs. (22) and (23) for both compressible and nearly incompressible materials, and thus requires no further treatment. In its most general form, the term $\widetilde{\mathcal{P}}$ is a convex function of the quantities $\mathcal{V}$ defined in the polyconvexity condition, c.f. Eq. (6). Instead of formulating $\widetilde{\mathcal{P}}$ directly in $\mathcal{V}$, it is commonly formulated in invariants of $\mathcal{V}$, c.f. Section 2.2. In this way, the objectivity and material symmetry conditions are fulfilled by construction. However, it also leads to a loss of information, as it is not possible to formulate a complete integrity basis in terms of polyconvex invariants for electro-elasticity, c.f. Remark 2.4.

Instead of choosing an analytical formulation for the term $\widetilde{\mathcal{P}}$, we aim to exploit the excellent approximation properties of neural networks [37] and use input convex feed-forward neural networks (ICNNs) [2]. In a nutshell, feed-forward neural networks (FFNNs) can be seen as a composition of several vector-valued functions, where the components of the vectors are referred to as nodes or neurons, and the function in each neuron is referred to as activation function. More explicitly, the FFNN with the vector-valued input $\boldsymbol{X} =: \boldsymbol{A}_0 \in \mathbb{R}^{n^{[0]}}$, output $\boldsymbol{Y} =: \boldsymbol{A}_{H+1} \in \mathbb{R}^{n^{[H+1]}}$, and H hidden layers is given by

$$\boldsymbol{A}_h = \sigma^{[h]}\left(\boldsymbol{W}^{[h]}\boldsymbol{A}_{h-1} + \boldsymbol{b}^{[h]}\right) \in \mathbb{R}^{n^{[h]}}, \quad h = 1, \ldots, H+1. \tag{41}$$

Here, $\boldsymbol{W}^{[h]} \in \mathbb{R}^{n^{[h]} \times n^{[h-1]}}$ are the weights and $\boldsymbol{b}^{[h]} \in \mathbb{R}^{n^{[h]}}$ the biases in each layer. Together, they form the set of parameters $\boldsymbol{p}$ of the neural network, which is optimized in the calibration process to fit a given dataset. In the layers $\boldsymbol{A}_h$, the scalar activation functions $\sigma^{[h]}$ are applied in a component-wise manner. By using a scalar-valued output, i.e. $n^{[H+1]} = 1$, and the special choice of activation functions as

- neuron-wise convex in the first layer
  (here: the *Softplus* function $\sigma^{[1]}(x) = s(x) = \log(1 + \exp(x))$),

- neuron-wise convex and non-decreasing in every subsequent layer
  (here: *Softplus* $\sigma^{[h]}(x) = s(x)$ with non-negative weights $\boldsymbol{W}_{ij}^{[h]} \geq 0$ for $h = 2, \ldots, H$),

- and scalar-valued, convex and non-decreasing in the output layer
  (here: $n^{[H+1]} = 1$ and a linear activation function $\sigma^{[H+1]}(x) = x$ with $\boldsymbol{W}_{ij}^{[H+1]} \geq 0$),

the FFNN is convex by construction and considered as an ICNN, see Klein et al. [47, Appendix A] for a proof. In the following, we use the short notation $\mathcal{SP}(\boldsymbol{X}; n^{[1]}, \ldots, n^{[H]})$ to describe FFNN architectures and $\mathcal{SP}^+(\boldsymbol{X}; n^{[1]}, \ldots, n^{[H]})$ to describe ICNN architectures, with input $\boldsymbol{X}$ and H hidden layers. For both FFNNs and ICNNs we apply (restricted) *Softplus* activation functions in all hidden layers, which are infinitely continuously differentiable, i.e. $\mathcal{SP}, \mathcal{SP}^+ \in \mathcal{C}^\infty(\mathbb{R}^{n^{[0]}}, \mathbb{R}^{n^{[H+1]}})$. A more extensive introduction to neural networks can be found in e.g. [1, 49].

Now, following Klein et al. [47], we use a set of invariants as described in Section 2 as input quantities of an ICNN, which represents the term $\widetilde{\mathcal{P}} := \mathcal{SP}^+$ as part of the internal energy e. The resulting potential

$$e\left(\boldsymbol{F}, \boldsymbol{d}_0\right) = \mathcal{P}(\boldsymbol{\mathcal{V}}) = \mathcal{SP}^+(\boldsymbol{\mathcal{I}}; n^{[1]}, \ldots, n^{[H]}) + \mathcal{P}_{\mathrm{vol}}(J) \tag{42}$$
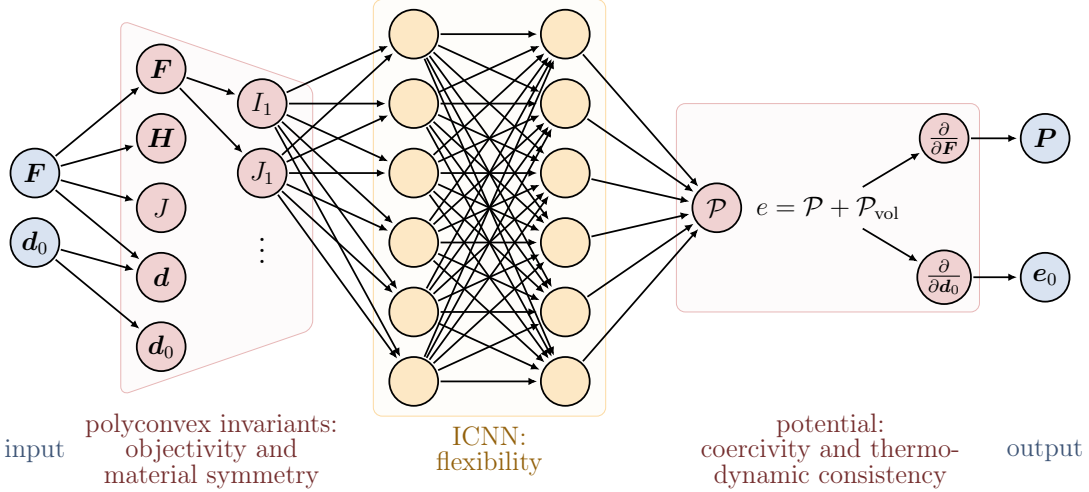
Figure 2: Illustration of the physics-augmented, ANN based constitutive model. Note that the polyconvexity of $\mathcal{P}$ must be preserved in every layer of the model. Figure generated with `https://tikz.net/neural_networks/`.

fulfills all constitutive requirements specified in Section 2. Here, $\boldsymbol{\mathcal{I}}$ denotes a vector of invariants, which corresponds to the arguments of $\widetilde{\mathcal{P}}$ as specified in Section 2.2. Note that for this special application also the first layer must be neuron-wise non-decreasing, as the invariants are non-linear functions of the quantities we want to be convex in, c.f. Klein et al. [47, Remark A.10]. Then, in particular the polyconvexity condition is fulfilled by using sets of convex invariants, and preserving the convexity by using input convex neural networks.

Then, as gradients of the energy potential e, see Eq. (5), the stress and electrical field can be computed via automatic differentiation, which is widely available in machine learning libraries. By construction, the conditions $\boldsymbol{P}(\mathbb{1}, \boldsymbol{0}) = \boldsymbol{0}$ and $\boldsymbol{e}_0(\mathbb{1}, \boldsymbol{0}) = \boldsymbol{0}$ are not fulfilled, and including these conditions in the model formulation would not be straightforward. However, as the data with which the model is calibrated fulfills these conditions, the model will approximate them after the calibration process. In Fig. 2, the overall structure and flow of this physics-augmented ANN model is illustrated.

In Eq. (42), the term $\mathcal{P}_{\text{vol}}$ depends on the volumetric behavior of the material and is prescribed as an analytical term, while $\mathcal{SP}^+$ is calibrated to data of a specific material. Throughout this work, we use calibration datasets of the form

$$D_i = \left\{ \left(\boldsymbol{F}^{i,1}, \hat{\boldsymbol{d}}_0^{i,1}; \hat{\boldsymbol{P}}^{i,1}, \hat{e}_0^{i,1}\right), \left(\boldsymbol{F}^{i,2}, \hat{\boldsymbol{d}}_0^{i,2}; \hat{\boldsymbol{P}}^{i,2}, \hat{e}_0^{i,2}\right), \dots \right\}, \qquad D = \bigcup_i D_i \qquad (43)$$

where D_i are different loading paths and D is the overall calibration dataset. Note that throughout this work all quantities $*$ are made dimensionless, which is indicated as $\hat{*}$, see Appendix A for further details. To calibrate the model $\square$ on the dataset D and find its parameters $\boldsymbol{p}$, we choose to minimize the loss function defined in terms of the mean squared error

$$\text{MSE}^{\square}(\boldsymbol{p}) = \sum_i \frac{1}{\#(D_i)} \frac{1}{w_i} \sum_j \left[\left\| \hat{\boldsymbol{P}}^{i,j} - \hat{\boldsymbol{P}}^{\square}\left(\boldsymbol{F}^{i,j}, \hat{\boldsymbol{d}}_0^{i,j}; \boldsymbol{p}\right) \right\|^2 + \left\| \hat{e}_0^{i,j} - \hat{e}_0^{\square}\left(\boldsymbol{F}^{i,j}, \hat{\boldsymbol{d}}_0^{i,j}; \boldsymbol{p}\right) \right\|^2 \right], \quad (44)$$

where $\#(D_i)$ denotes the number of data points in D_i and w_i is the norm

$$w_i = \frac{1}{\#(D_i)} \sum_j \left\| \hat{\boldsymbol{P}}^{i,j} \right\|. \qquad (45)$$

13

Note that the weights w_i are introduced in order to balance the importance of different load paths within the MSE, see [23]. In contrast to the dataset introduced in Eq. (43), the homogenization of composites and metamaterials not only allows to compute $\boldsymbol{P}$ and $\boldsymbol{e}_0$, but also the internal energy e. Basically, this information could also be included in the loss function. However, previous examinations showed that this hardly increases the prediction quality of the model, c.f. [22, 47]. Also, this would lead to a loss of generality, as experimental investigations only provide the data introduced in Eq. (43). Therefore, the internal energy is calibrated only through its gradients, which can be considered as a variant of the Sobolev training strategy [91, 92].

4 Application to a transversely isotropic potential

As a first proof of concept, we apply the ANN based constitutive model proposed in Section 3 to fitting an analytical electro-elastic potential with transversely isotropic material symmetry. Furthermore, we investigate how the consideration of constitutive requirements in the model formulation influences its properties, especially generalization and flexibility.

4.1 Data generation

The transversely isotropic potential considered in this section includes the invariants described in Section 2.2.2 for this particular material symmetry group. Specifically, the following invariant-based additive decomposition is considered

$$e^{\text{ti}}(\boldsymbol{\mathcal{U}}) = \mathcal{P}^{\text{ti}}(\boldsymbol{\mathcal{V}}) = \widetilde{\mathcal{P}}(\boldsymbol{\mathcal{I}}^{\text{iso}}) + \widetilde{\mathcal{P}}(\boldsymbol{\mathcal{J}}^{\text{ti}}) + \mathcal{P}_{\text{vol}}(J) \,, \tag{46}$$

with

$$\widetilde{\mathcal{P}}(\boldsymbol{\mathcal{I}}^{\text{iso}}) = \frac{\mu_1}{2} \bar{I}_1 + \frac{\mu_2}{2} \bar{I}_2^* - \mu_3 \log J + \frac{1}{2\varepsilon_1} \frac{I_5}{J} \,,$$

$$\widetilde{\mathcal{P}}(\boldsymbol{\mathcal{J}}^{\text{ti}}) = \frac{\mu_3}{2} \left(\frac{(J_1^{\text{ti}})^{a_1}}{a_1} + \frac{(J_2^{\text{ti}})^{a_2}}{a_2} \right) + \frac{1}{2\varepsilon_2} J_3^{\text{ti}} \,, \tag{47}$$

$$\mathcal{P}_{\text{vol}}(J) = \frac{\lambda}{2} (J - 1)^2 \,,$$

where $\mu_1, \mu_2, \mu_3, \lambda$ represent mechanical material parameters with units of stress (Pa) and $\varepsilon_1, \varepsilon_2$ electric permittivity-type material parameters with units of $\text{CV}^{-1}\text{m}^{-1}$. In particular, here the following specific values are used

$$\begin{aligned} \mu_2 &= \mu_1 \,, & \mu_3 &= 3\mu_1 \,, & a_1 &= 2 & a_2 &= 2 \,, \\ \lambda &= 10^3 \mu_1 \,, & \varepsilon_2 &= 2\varepsilon_1 \,, & \boldsymbol{n} &= \begin{pmatrix} 0 & 0 & 1 \end{pmatrix}^T \,. \end{aligned} \tag{48}$$

Note that usually the difference between the values of the mechanical parameters $\mu_1, \mu_2, \mu_3, \lambda$ and the electro-mechanical parameters $\varepsilon_1, \varepsilon_2$ can be of several orders of magnitude. This scaling difference can entail difficulties for the construction of a suitable neural network capturing both underlying physics, namely mechanical and electro-mechanical (in fact, it is challenging for any numerical optimization approach for parameter fitting). With the aim of circumventing this potential drawback, we make use of the energy scaling procedure described in Appendix A.

While real-world investigations of material behavior require (cumbersome) experiments, this analytical potential can either be directly evaluated for a given deformation gradient $\boldsymbol{F} \in \text{GL}^+(3)$ and electric displacement field $\boldsymbol{d}_0 \in \mathbb{R}^3$, or be (numerically) equilibrated for stress-strain states such as uniaxial tension, biaxial tension, pure shear, etc. Here, we choose the former approach to generate

data for the calibration of machine learning based constitutive models. In order to examine some special model properties, the global behavior of Eq. (46) is sampled for a wide range of physically admissible deformations, which are described in Appendix B. Altogether, this results in a fairly large dataset with 1.5 million points. As we will show, such a large dataset may not be necessary to calibrate (physics-augmented) machine learning models, however, it will be useful to examine some specific model properties. Finally, for this specific example, based on the analytical potential in Eqs. (46) and (47), for each deformation gradient tensor $\boldsymbol{F}$ and electric displacement field $\boldsymbol{d}_0$, we simply evaluate the derivatives of the analytical potential $e^{\text{ti}}(\boldsymbol{\mathcal{U}})$ according to Eq. (5) in order to obtain their respective work conjugates $\boldsymbol{P}$ and $\boldsymbol{e}_0$, which are required for evaluating the mean squared error as defined in Eq. (44).

4.2 Model calibration

Model A. This is the *physics-augmented*, invariant-based model as proposed in Section 3, which fulfills all of the constitutive requirements as described in Section 2. As we assume transversely isotropic, nearly incompressible material behavior, we use the invariant vector

$$\boldsymbol{\mathcal{I}} = \left(\bar{I}_1, \ \bar{I}_2, \ J, \ -J, \ \hat{I}_5, \ J_1^*, \ J_2^* \right) \in \mathbb{R}^7 \tag{49}$$

with the invariants as described in Section 2.2, and the scaling as described in Appendix A. The transversely isotropic invariants are slightly adapted according to $J_1^* = J_1 + 0.35 \, I_1$ and $J_2^* = J_2 + 0.35 \, I_2$, which can also be obtained by replacing the structural tensor from Eq. (32) with $\boldsymbol{G}^{\text{ti}} = \text{diag}\,(0.35, \, 0.35, \, 1)$. Furthermore, here all invariants are polyconvex, whereas in Eq. (47) the non-polyconvex isochoric invariant $\bar{I}_2^*$ is used, c.f. Eq. (24). As the invariants are non-linear in the quantities of the polyconvexity condition, also the first layer of the ICNN must have non-decreasing activation functions and thus non-negative weights for the *Softplus* function, c.f. Klein et al. [47, Remark A.10]. The only exception is J, which is the only invariant quantity included in the polyconvexity condition, c.f. Eq. (6). Thus, the weights in the first layer which act on the invariant J may be positive or negative. This is pragmatically implemented by adding the additional invariant $-J$.

With the choice of invariants as specified in Eq. (49), the approximation of the analytical potential from Eq. (46) does *not* reduce to approximating a (mostly) linear function, as the input quantities of the ICNN differ from the ones used in Eq. (46). In particular, the invariant J_3 is not used and all other invariants differ slightly in their concrete form. When choosing all the invariants as they appear in Eq. (46), the ICNN would model a linear function in most of the invariants, which would be trivial and thus not be a good benchmark case. In fact, for this case, even significantly smaller calibration datasets than the ones used throughout this section would yield a perfect approximation of Eq. (46).

For this model, we choose two network architectures: model A^1 consisting of only one hidden layer with 8 nodes ($H = 1, n^{[1]} = 8$) and model A^2 consisting of two hidden layers with 16 nodes in each layer ($H = 2, n^{[h]} = 16$), for which we use the short notations $\text{A}^1 = \mathcal{SP}^+(\boldsymbol{\mathcal{I}}; 8)$ and $\text{A}^2 = \mathcal{SP}^+(\boldsymbol{\mathcal{I}}; 16, 16)$, respectively. The former has a total amount of 73 free parameters, the latter has 417 free parameters.

Model B. In addition to the physics-augmented model from Section 3, we introduce a second, *uninformed* machine learning model, which includes considerably less mathematical structure, i.e., it incorporates fewer physical requirements. For this purpose, we use a FFNN without any restrictions on the activation functions and weights, which is thus not convex. Here, we also use the *Softplus*

activation functions, but with unrestricted weights. Now, we directly map $\boldsymbol{C} = \boldsymbol{F}^T \boldsymbol{F}$ and $\boldsymbol{d}_0$ to $\boldsymbol{P}$ and $\boldsymbol{e}_0$, i.e.

$$(\boldsymbol{P},\,\boldsymbol{e}_0) = \mathcal{SP}(\boldsymbol{C},\,\boldsymbol{d}_0;\,n^{[1]},\ldots,n^{[H]})\,. \tag{50}$$

Note that in contrast to the model proposed in Section 3, the neural network in the above equation is *not* used to model an internal energy, c.f. Eq. (42), but directly outputs the mechanical stress field and the electrical field. Since formulated in $\boldsymbol{C}$, this model is objective, but beside that it does not fulfill any of the other constitutive requirements introduced in Section 2. In fact, it is not even hyperelastic, i.e., it is not necessarily thermodynamically consistent.

For this model, we also choose two network architectures: model B^1 consisting of two hidden layers with 16 nodes in each layer ($H = 2, n^{[h]} = 16$) and model B^2 consisting of four layers with 64 nodes in each layer ($H = 4, n^{[h]} = 64$), for which we use the short notations $\mathrm{B}^1 = \mathcal{SP}(\boldsymbol{C},\boldsymbol{d}_0; 16, 16)$ and $\mathrm{B}^2 = \mathcal{SP}(\boldsymbol{C},\boldsymbol{d}_0; 64, 64, 64, 64)$, respectively. The former has a total amount of 684 free parameters, the latter has $14,092$ free parameters. In both cases, the output layer consists of a 12-dimensional layer with linear activation functions.

Calibration details. As described above, the overall dataset D comprises of 1.5 million data points. It is divided into subsets D_i, where each one consists of a fixed deviatoric direction, c.f. Appendix B. Overall, this results in $300,000$ sub-datasets with 50 data points each. In this way, we are able to weight the MSE of the different loading paths according to Eq. (44), which is important as the magnitude of the paths greatly differs. The calibration datasets are composed of different amounts of sub-datasets $n_{\mathrm{data}} = 2^n$, $n = 4, 5, \ldots, 11$, resulting in calibration dataset sizes between 400 and $102,400$ points. For each calibration dataset size n_{data}, each model calibration was initialized 10 times. For each initialization, different random sub-datasets were used for the calibration dataset, by ordering the sub-datasets from 1 to $300,000$ and generating random sets of integers to choose out of them. Also, for each initialization, the model parameters, i.e., the weights and biases, were initialized randomly with the default settings of TensorFlow. For the following investigations the MSE after the calibration process is evaluated on the overall dataset for all 1.5 million data points, meaning that the test dataset equals the overall dataset.

The models are implemented in TensorFlow 2.5.0, using Python 3.9.9. The optimization is carried out using the ADAM algorithm with default settings, except for the learning rate which is set to 0.005. The calibration is carried out for $5,000$ iterations (epochs), which showed to be sufficient for converged results. The full batch of training data is used with a batch size of 400. For the reproducibility of the results, in addition to the data, we provide the calibrated parameters of the models on the GitHub repository `https://github.com/CPShub/sim-data`. For general details on the reproducibility of the models, see also Klein et al. [47, Sect. 4.2].

4.3 Model evaluation

In Fig. 3, the results of all different model calibrations are shown, with the logarithm of the number of sub-datasets n_{data} used for calibration on the horizontal axis and the logarithmic MSE of the overall dataset on the vertical axis. The two invariant-based models A are visualized in red colors, while the uninformed models B are displayed in blue colors. As the calibration was initialized multiple times for each n_{data}, the corresponding MSEs form an area containing all results, with the median visualized with a continuous line.

For the model B, the small network architecture B^1 does not provide enough flexibility, consequently the MSE stagnates at a relatively high value around 10^{-1}. For the bigger network structure B^2, however, the MSE decreases consistently with increasing calibration dataset size, and could
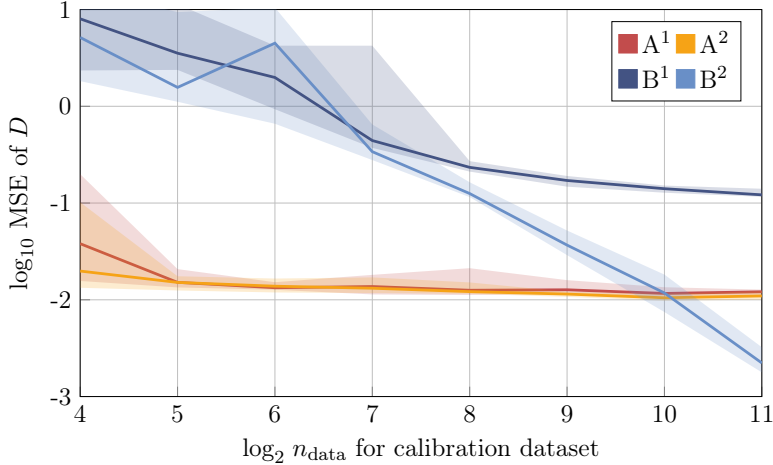
16

Figure 3: Transversely isotropic potential, evaluation of the models. $A^1 = \mathcal{SP}^+(\boldsymbol{\mathcal{I}}; 8)$ and $A^2 = \mathcal{SP}^+(\boldsymbol{\mathcal{I}}; 16, 16)$ denote the physics-augmented models, while $B^1 = \mathcal{SP}(\boldsymbol{C}, \boldsymbol{d}_0; 16, 16)$ and $B^2 = \mathcal{SP}(\boldsymbol{C}, \boldsymbol{d}_0; 64, 64, 64, 64)$ denote the uninformed models with less mathematical structure. For the different models, the MSE of the overall dataset D is evaluated depending on the number n_{data} of sub-datasets D_i used for calibration. The spreads of all 10 initializations are shown by shaded areas, whereas the continuous lines indicate the medians.

probably decrease even further with more data. In contrast to that, the invariant-based approaches can cope with far smaller network architectures and calibration datasets. In fact, increasing the network size from model A^1 to A^2 hardly improves the model quality. However, the MSE converges quite fast to around 10^{-2} and does not further decrease for an increasing calibration dataset or model architecture. For both models, the spread of the MSE for multiple initializations is decreasing for increasing calibration datasets. This was also observed in Klein et al. [47], where multiple initializations of the same machine learning model architecture resulted in quite similar MSEs of the test dataset.

Out of the $300,000$ sub-datasets D_i, one load case is now used to evaluate the mechanical stress and electrical field for both calibrated models. As shown in Fig. 4 in the top row, in this specific load case, all three components of the electrical displacement field $\boldsymbol{d}_0$ are non-zero but constant, while the deformation gradient consists of an increasing value of F_{11} and strong shear components.

The invariant-based model A^1 is evaluated for $n_{\text{data}} = 32 = 2^5$, the uninformed model B^2 is evaluated for $n_{\text{data}} = 2,048 = 2^{11}$. Each model was calibrated one time, which resulted in a $\log_{10}$ MSE of the overall dataset of -1.77 for A^1 and -2.76 for B^2. The $\log_{10}$ MSE for the single load case visualized below is -1.63 for A^1 and -3.26 for B^2. Therefore, this case is representative for the global $\log_{10}$ MSE of the model A^1, while it overestimates the prediction quality of B^2.

In the middle row of Fig. 4, the resulting stress and electrical field for model A^1 are shown. For both quantities, all components are activated and highly nonlinear. Beside slight deviations, e.g., in the P_{33} component, this very small, physics-augmented model shows excellent results for all components. In the bottom row of Fig. 4, the results for the model B^2 are shown. This fairly large, uninformed model also shows excellent results for both the mechanical stress and the electrical field, even outperforming the results of A^1. Overall, both models perform excellent on this really challenging evaluation case.
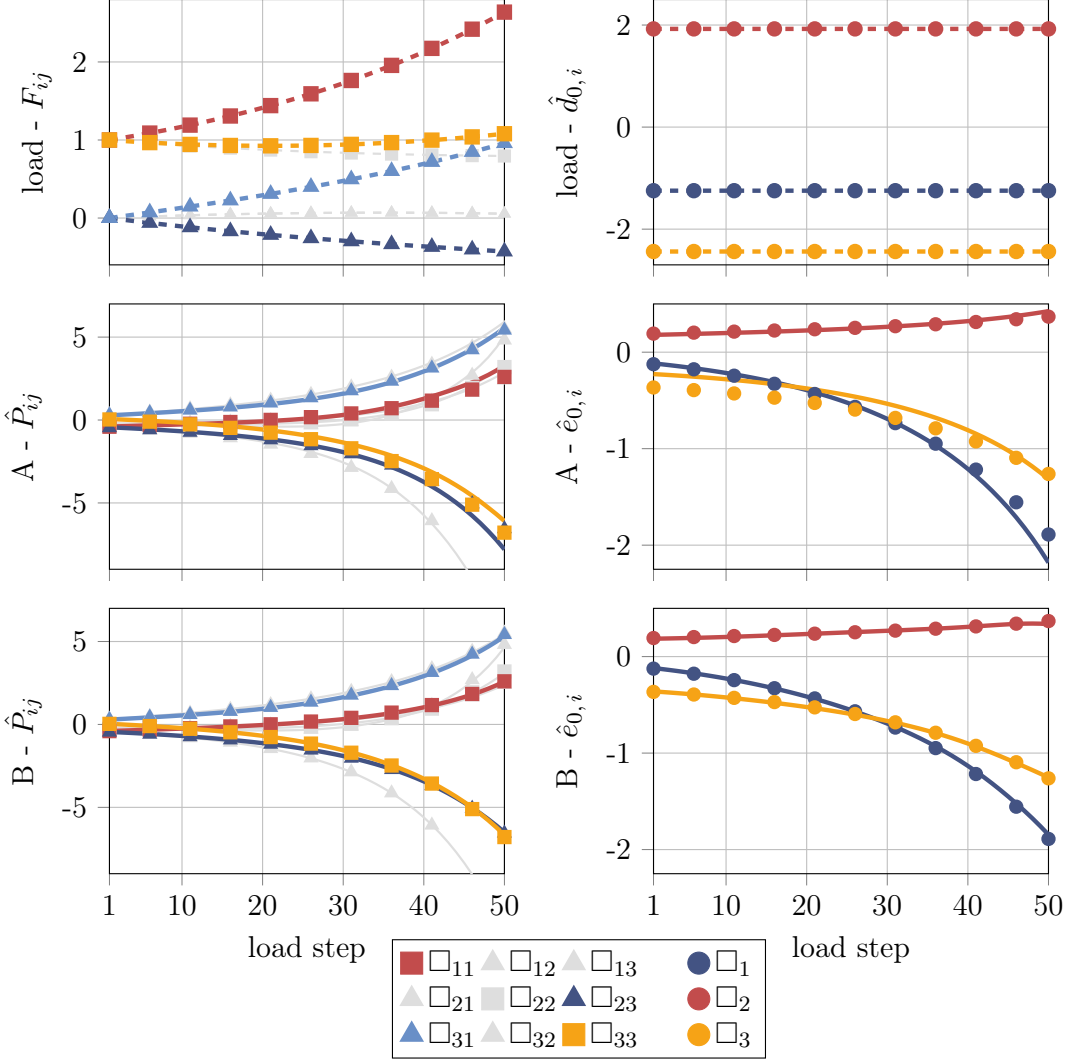
Figure 4: Transversely isotropic potential, load case and evaluation of the models. Points depict data from the analytical potential, while continuous lines depict the evaluation of the models. A denotes the physics-augmented model A[1], while B denotes the uninformed model B[2]. All quantities are dimensionless.

4.4 Influence of the physical augmentation on the model

Overall, the invariant-based, physics-augmented model A can cope with much smaller network architectures and calibration datasets than the uninformed model B. However, it is less flexible and thus has a slightly worse prediction quality for very big calibration datasets. This shows two effects that including constitutive requirements has on the model: First of all, it provides a pronounced mathematical structure which helps to generalize the model very fast. By including fundamental physical principles in the model, such as the second law of thermodynamics, the model behavior is already specified to some amount, thus simplifying the calibration process for a specific material. In that sense, constitutive conditions can be seen as an *inductive bias* [33].

While the use of invariants provides the model with a lot of structure and fulfills several constitutive requirements by construction, this is also a potential bottleneck: in a purely mechanical framework it is possible to formulate a complete functional basis in terms of (polyconvex) invariants for the transverse isotropy used in this example [98]. However, this is not possible for all symmetry

groups, especially for electro-mechanically coupled material behavior, c.f. Remark 2.4. Overall, the invariant layer may lead to a loss of information: even when it is possible to construct a complete functional basis in invariants for a symmetry group, some of its elements may not be polyconvex and can thus not be used. Also, for some anisotropy classes, no complete functional basis in invariants is known at all [98]. This loss of information can only be partially compensated by the flexibility of the neural network. This leads to the second point: the loss of flexibility. Constitutive requirements often restrict the possible function space of the model, e.g., when loosing information in the invariant layer or when assuming an internal energy as *convex*.

However, the restrictions made in this work are either physically well based, e.g., the use of an internal energy which ensures the second law of thermodynamics, or they have a strong mathematical motivation, such as the polyconvexity condition which ensures material stability. Therefore, they should not be seen as strong restrictions of the model behavior, rather, they lead to reliable, i.e., physically sensible, model predictions, while also improving the generalization properties of the model. Thus, in the trade-off between structure and flexibility, structure should be prioritized as far as possible. Only if it is inevitable, only when more flexibility is required, should the structure of the model be weakened, e.g., by fulfilling some constitutive requirements only in an approximate fashion, c.f. [47]. In terms of constitutive requirements, the invariant based model proposed in Section 3 has the same amount of structure as most analytical models found in literature, c.f. [85]. Only for some analytical models, it is possible to arrive at even more interpretable formulations in the sense that the model parameters have a physical meaning, such as shear and compression modulus for the hyperelastic Hencky model [34, 35, 64, 65].

That the model proposed in Section 3 fulfills fundamental physical principles is the first reason to trust its predictions – the second one is its excellent prediction of test cases. Generally, it is not sufficient to calibrate the model to a given dataset, it is just as important to evaluate it for load paths which are not included in the calibration dataset. Only in this way the *generalization* of the model can be assessed. In this academic example it is straightforward to evaluate the global behavior of the potential Eq. (46), and thus to assess the generalization of the proposed machine learning model on a global scale, c.f. Fig. 3. However, this is in general not possible due to strong practical limitations of experimental investigations [4] or the computational effort of numerical investigations of complex microstructures [42]. In practice, usually only small test datasets can be created. The deformations used for this should be as general as possible, e.g., by combining both normal and shear components in the deformation gradient, c.f. Fig. 4, and within the deformation range in which the model will be used. Thereby, it can be assumed that the test case is representative for the global behavior of the material. When the model is then able to predict the material behavior for this test case it can be assumed that it can generally predict its global behavior. Note that this strategy is well known and usually implemented in machine learning, as datasets are typically separated into calibration and test sets [1].

Due to the reasons mentioned above, uniform sampling of the input space will not be applied in the following sections. It should be noted that some machine learning approaches directly act on global force and displacement data generated with finite element simulations [25, 43]. However, these methods are restricted to data generated with FE simulations and are thus less general. Instead, in the following sections, deformation scenarios which are commonly applied in experimental investigations will be used for the calibration dataset, such as uniaxial tension, and additional test cases with general deformation modes, c.f. [22].
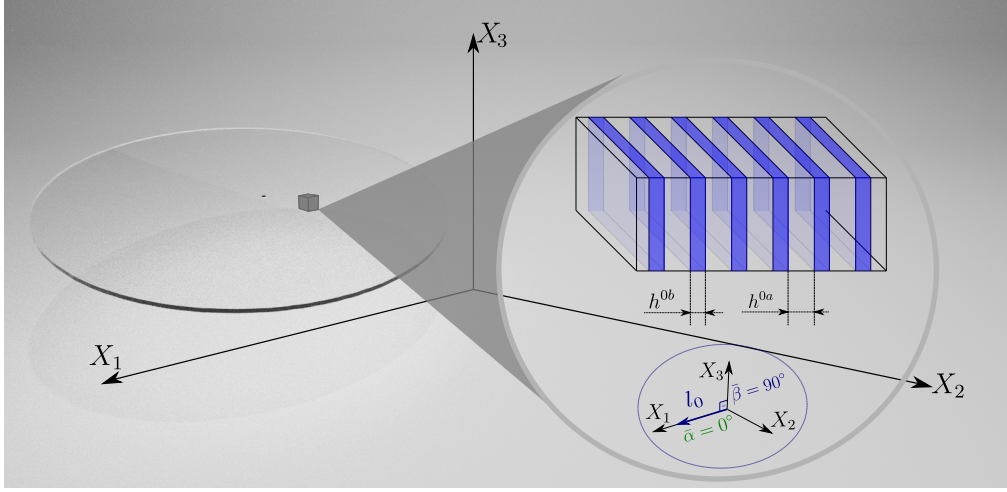
Figure 5: Description of the microstructure of the rank-one laminate: the purple constituent corresponds to phase b, inserted within phase a according to a lamination orientation perpendicular to the vector $\boldsymbol{l}_0$.

5 Application to an analytically homogenized rank-one laminate

After the more academic example in the previous section, the proposed model is now applied to data of an analytically homogenized rank-one laminate. In doing so, we demonstrate the applicability of the model to the challenging effective behaviors of electro-mechanical composite materials.

5.1 Data generation

The structure of a biphasic rank-one laminated DE composite is comprised of constituents or phases a and b, as illustrated in Fig. 5, c.f. [59]. The two phases a and b occupy volume fractions $c^a = h_0^a / \left(h_0^a + h_0^b \right)$ and $c^b = 1 - c^a$, respectively, where h_0^a and h_0^b denote the thicknesses of the phases in the initial configuration $\mathcal{B}_0$ (with small h_0^a, h_0^b to comply with homogenization theory). The interface between both phases is characterised by the normal vector $\boldsymbol{l}_0$, which is spherically parametrized as $\boldsymbol{l}_0 = \left(\sin \bar{\beta} \cos \bar{\alpha}, \ \sin \bar{\beta} \sin \bar{\alpha}, \ \cos \bar{\beta} \right)^T$.

For the homogenization, we assume the existence of the microscopic fields $\boldsymbol{F}^a, \boldsymbol{d}_0^a$ and $\boldsymbol{F}^b, \boldsymbol{d}_0^b$ in each phase a and b. The internal energy density of both phases a and b, namely $e^{a,b}(\boldsymbol{F}^{a,b}, \boldsymbol{d}_0^{a,b})$, admits a decomposition similar to that in Eq. (21), but in terms of invariants of either $\{\boldsymbol{F}^a, \boldsymbol{d}_0^a\}$ or $\{\boldsymbol{F}^b, \boldsymbol{d}_0^b\}$, namely

$$e^{a,b}(\boldsymbol{F}^{a,b}, \boldsymbol{d}_0^{a,b}) = \mathcal{P}^{a,b}(\boldsymbol{\mathcal{V}}^{a,b}) = \widetilde{\mathcal{P}}^{a,b}(\boldsymbol{\mathcal{I}}^{a,b}) + \mathcal{P}_{\text{vol}}^{a,b}(J^{a,b}) \,. \tag{51}$$

Here, the specific form of both contributions in Eq. (51) is assumed as

$$
\begin{aligned}
\widetilde{\mathcal{P}}^a(\boldsymbol{\mathcal{I}}^a) &= \frac{\mu_1}{2} I_1^a + \frac{\mu_2}{2} I_2^a + \frac{I_5^a}{2\varepsilon J^a} \,, & \mathcal{P}_{\text{vol}}^a(J^a) &= \frac{\lambda}{2}(J^a - 1)^2 \,, \\
\widetilde{\mathcal{P}}^b(\boldsymbol{\mathcal{I}}^b) &= f_m\left(\frac{\mu_1}{2} I_1^b + \frac{\mu_2}{2} I_2^b \right) + \frac{I_5^b}{2 f_e \varepsilon J^b} \,, & \mathcal{P}_{\text{vol}}^b(J^b) &= f_m \frac{\lambda}{2}(J^b - 1)^2 \,,
\end{aligned}
\tag{52}
$$

where f_m, f_e represent the mechanical and electro-mechanical contrast parameters relating the material properties of phases a and b. Clearly, both matrix and inclusion constituents are described by means of isotropic internal energy densities. Specifically, we use of the following material parameters

$$\mu_2 = 0.1\mu_1 \,, \qquad \lambda = 50\mu_1 \,, \qquad f_m = 20 \,, \qquad f_e = 2 \,, \qquad c_a = 0.5 \,, \qquad \boldsymbol{l}_0 = \begin{pmatrix} 0 & 0 & 1 \end{pmatrix}^T \,. \tag{53}$$

The detailed derivation of the homogenized relationship between the microscopic fields $\boldsymbol{F}^{a,b}, \boldsymbol{d}_0^{a,b}$, as well as $e^{a,b}$ and $\boldsymbol{P}^{a,b}, \boldsymbol{e}_0^{a,b}$, and their macroscopic counterparts $\boldsymbol{F}, \boldsymbol{d}_0, e, \boldsymbol{P}, \boldsymbol{e}_0$ can be found in Appendix C. Note that the scaling procedure described in Appendix A with respect to the material parameters μ_1, ε is carried out in order to facilitate the calibration of the ANN based constitutive model by reducing the significant dissimilarity between mechanical and electro-mechanical parameters.

For the data generation, the following 10 load cases for the macroscopic fields $\boldsymbol{F}$ and $\boldsymbol{d}_0$ are considered: (1) purely mechanical uniaxial tension, (2) purely mechanical pure shear load, (3–4) the minimum mechanical value for uniaxial tension, and then two datasets with an electric displacement field applied in X_1 and X_3 direction, respectively, (5–6) the maximum mechanical value for uniaxial tension, and then two datasets with an electric displacement field applied in X_1 and X_3 direction, respectively, (7–8) the minimum mechanical value for shear load, and then two datasets with an electric displacement field applied in X_1 and X_3 direction, respectively, and (9–10) the maximum mechanical value for shear load, and then two datasets with an electric displacement field applied in X_1 and X_3 direction, respectively. With each single load case consisting of 100 data points, this results in an overall calibration dataset size of $1,000$ datapoints. For the explicit definition of the deformation gradients of these load cases, see [22]. In addition, a biaxial test case and a mixed shear-tension test case were generated, both with variable electric displacement fields.

5.2   Model calibration

For the invariant-based ANN model proposed in Section 3, we use the input

$$\boldsymbol{\mathcal{I}} = \left(I_1, \, I_2, \, J, \, -J, \, \hat{I}_4, \, \hat{I}_5, \, J_1^{\text{ti}}, \, J_2^{\text{ti}}, \, \hat{J}_3^{\text{ti}} \right) \in \mathbb{R}^9 \,, \tag{54}$$

with the invariants as described in Section 2.2, and the scaling as described in Appendix A. The input consists of both isotropic and transversely isotropic invariants. For the ICNNs, we choose two network architectures: one consisting of only one hidden layer with 8 nodes ($H = 1, n^{[1]} = 8$) and one consisting of two hidden layers with 16 nodes in each layer ($H = 2, n^{[h]} = 16$), for which we use the short notations $\mathcal{SP}^+(\boldsymbol{\mathcal{I}}; 8)$ and $\mathcal{SP}^+(\boldsymbol{\mathcal{I}}; 16, 16)$, respectively. The former has a total amount of 89 free parameters, the latter has 449 free parameters. Each model architecture was initialized three times, using different randomly initialized model parameters each time. The calibration is carried out for $2,500$ epochs. The full batch of training data is used with TensorFlow's default learning rate and default batch size. For the remaining calibration details, see Section 4.2.

5.3   Model evaluation

In Table 1, the MSEs of the different model initializations are provided. Both architectures show excellent results for the calibration dataset with slightly worse MSEs for the test dataset. Overall, the model with the smaller network architecture is already sufficiently flexible, in fact, it performs even better on the test dataset than the model with the bigger architecture.

In Figs. 6 and 7, the evaluations of the two test cases are shown for the model with the best test MSE. The first test case in Fig. 6 comprises of a biaxial deformation gradient and a variable electric displacement field. The second test case in Fig. 7 comprises of a mixed shear-tension deformation gradient and a variable electric displacement field. Both cases are highly challenging and especially the mixed case represents a general deformation case, extrapolating the model to data not seen in the calibration dataset. For both cases the model shows excellent results, with only slight deviations for high biaxial compression values in Fig. 6.

| Architecture | $\log_{10}$ MSE | |
	calibration	test
$\mathcal{SP}^+(\mathcal{I}; 8)$	-2.85	-1.78
—"—	-2.87	-1.77
—"—	-2.77	-1.76
$\mathcal{SP}^+(\mathcal{I}; 16, 16)$	-2.81	-1.61
—"—	-2.76	-1.60
—"—	-2.75	-1.59

Table 1: MSEs of the calibrated ANN based models for the rank-one laminate.
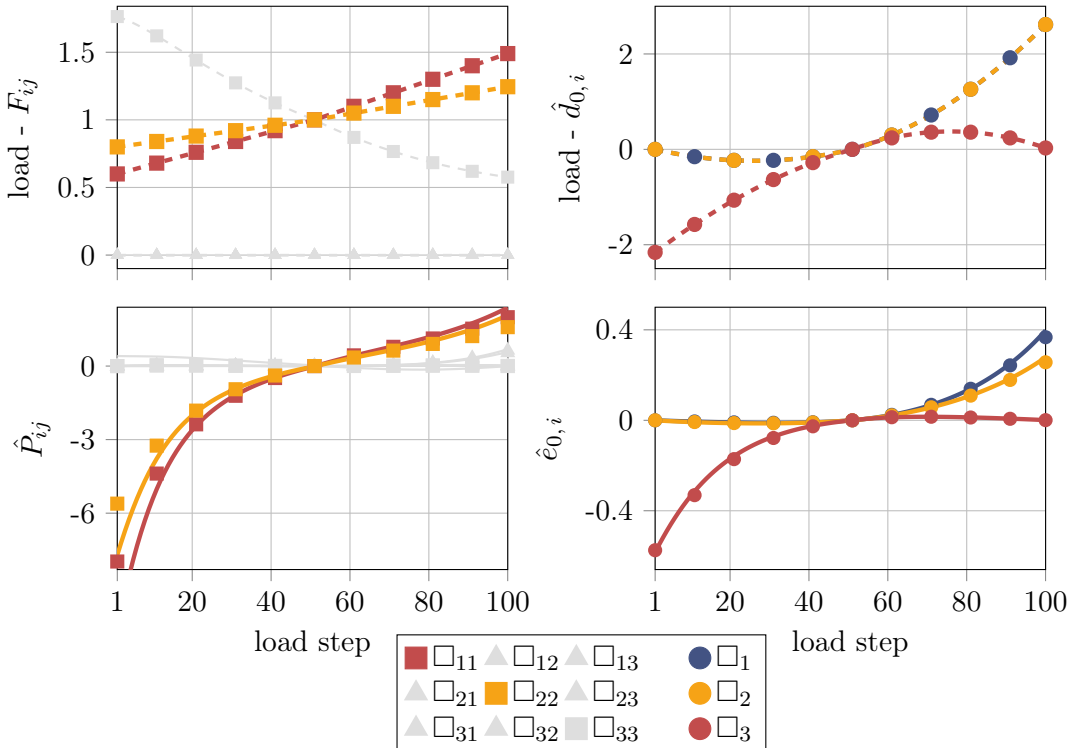
Figure 6: Evaluation of the biaxial test case for the rank-one laminate. Points depict homogenization data, while lines depict the evaluation of the machine learning model. All quantities are dimensionless.

Thus, this example shows how the physics-augmented neural network constitutive model is able to generalize with small amounts of data, and that even very small network architectures can provide sufficient flexibility.

6 Application to a numerically homogenized cubic metamaterial

Finally, a more complex microstructure than the one in Section 5 is considered. Thus, the homogenization of the effective material behavior of the cubic metamaterial, which serves as data for the model calibration, is carried out numerically. This shows the application of the proposed machine learning model to cases where no analytical homogenization is possible, and the straightforward applicability towards other symmetry groups.
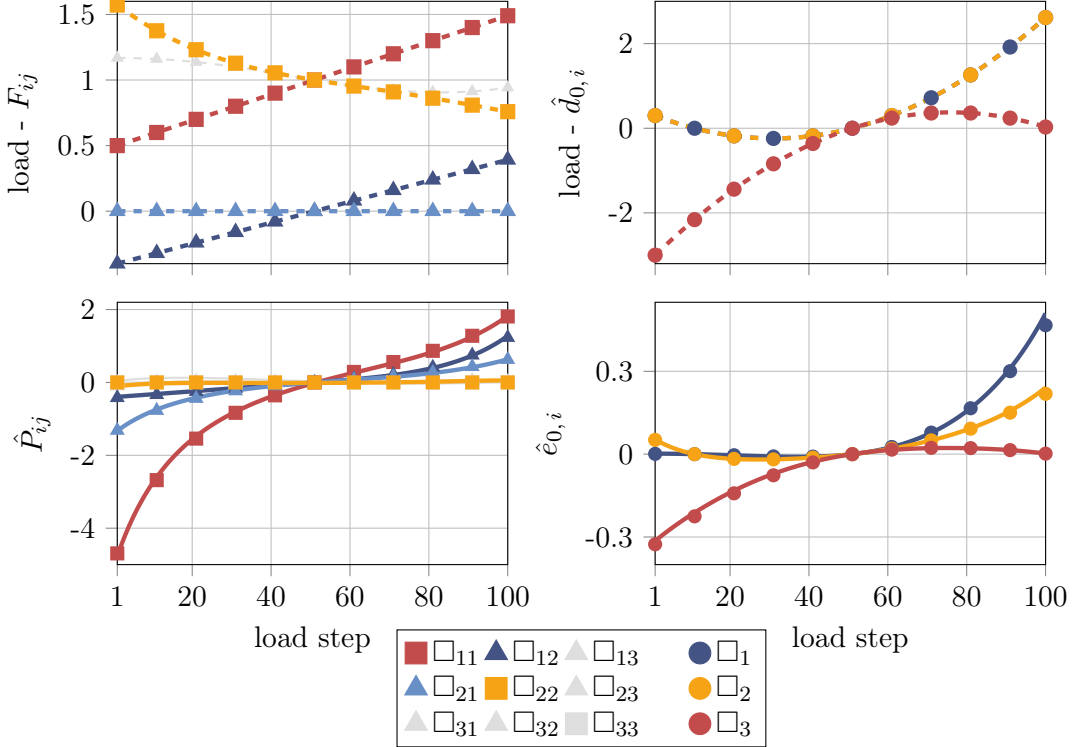
Figure 7: Evaluation of the shear-tension test case for the rank-one laminate. Points depict homogenization data, while lines depict the evaluation of the machine learning model. All quantities are dimensionless.

6.1 Data generation

We consider a metamaterial with cubic symmetry, which is characterized by a representative volume element (RVE) with a cubic matrix and a spherical inclusion, see Fig. 8. The radius of the inclusion is a quarter of the cell length.

In this case, the spatial and material coordinates in the RVE are denoted as $\boldsymbol{x}_\mu : \mathcal{B}_\mu \to \mathbb{R}^3$ and $\boldsymbol{X}_\mu : \mathcal{B}_{0_\mu} \to \mathbb{R}^3$, respectively, where $\mathcal{B}_\mu$ represents the deformed configuration of the undeformed RVE configuration $\mathcal{B}_{0_\mu}$. In addition, we assume the existence of a microscopic electric potential $\varphi_\mu : \mathcal{B}_{0_\mu} \to \mathbb{R}$. With this, it is possible to define the deformation gradient tensor and the electric field in the RVE, denoted as $\boldsymbol{F}_\mu$ and $\boldsymbol{e}_{0_\mu}$, as

$$\boldsymbol{F}_\mu = \frac{\partial \boldsymbol{x}_\mu}{\partial \boldsymbol{X}_\mu}, \qquad \boldsymbol{e}_{0_\mu} = -\frac{\partial \varphi_\mu}{\partial \boldsymbol{X}_\mu}. \tag{55}$$

The macroscopic deformation gradient $\boldsymbol{F}$ and electric field $\boldsymbol{e}_0$ are defined in terms of volume averages of their microscopic counterparts $\boldsymbol{F}_\mu$ and $\boldsymbol{e}_{0_\mu}$ according to, c.f. [62],

$$\boldsymbol{F} = \frac{1}{V_\mu} \int_{\mathcal{B}_{0_\mu}} \boldsymbol{F}_\mu (\boldsymbol{X}_\mu) \, dV_\mu = \frac{1}{V_\mu} \int_{\partial\mathcal{B}_{0_\mu}} \boldsymbol{x}_\mu (\boldsymbol{X}_\mu) \otimes \boldsymbol{n}_{0_\mu} \, dV_\mu,$$

$$\boldsymbol{e}_0 = \frac{1}{V_\mu} \int_{\mathcal{B}_{0_\mu}} \boldsymbol{e}_{0_\mu} (\boldsymbol{X}_\mu) \, dV_\mu = \frac{1}{V_\mu} \int_{\partial\mathcal{B}_{0_\mu}} \varphi_\mu (\boldsymbol{X}_\mu) \boldsymbol{n}_{0_\mu} \, dV_\mu. \tag{56}$$

Likewise, the macroscopic stress and electric displacement fields $\boldsymbol{P}$ and $\boldsymbol{d}_0$, respectively, can be
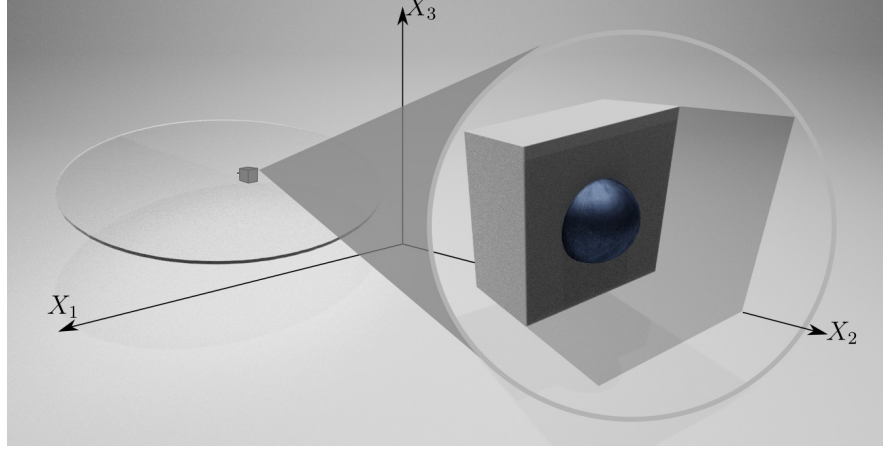
Figure 8: RVE for the cubic metamaterial, comprising a cubic matrix with spherical inclusion.

defined as averages of their microscopic counterparts, namely $\boldsymbol{P}_\mu$ and $\boldsymbol{d}_{0_\mu}$, as

$$\boldsymbol{P} = \frac{1}{V_\mu} \int_{\mathcal{B}_{0_\mu}} \boldsymbol{P}_\mu \, dV_\mu \,, \qquad \boldsymbol{d}_0 = \frac{1}{V_\mu} \int_{\mathcal{B}_{0_\mu}} \boldsymbol{d}_{0_\mu} \, dV_\mu \,. \tag{57}$$

For a detailed derivation of the computational homogenization procedure for this type of microstructure, the reader is referred to Appendix D. Here, we just want to further introduce the microscopic material models required for the homogenization. The microscopic internal energy density $e_\mu(\boldsymbol{F}_\mu, \boldsymbol{d}_{0_\mu})$ admits a decomposition similar to that in Eq. (21), but in terms of invariants of microscopic fields, namely

$$e_\mu(\boldsymbol{F}_\mu, \boldsymbol{d}_{0_\mu}) = \mathcal{P}_\mu(\boldsymbol{\mathcal{V}}_\mu) = \widetilde{\mathcal{P}}(\boldsymbol{\mathcal{I}}_\mu) + \mathcal{P}_{\mathrm{vol}_\mu}(J_\mu) \,. \tag{58}$$

The specific form of both contributions in Eq. (58) depends on the material coordinate $\boldsymbol{X}_\mu \in \mathcal{B}_{0_\mu}$ according to

$$\widetilde{\mathcal{P}}_\mu(\boldsymbol{X}_\mu, \boldsymbol{\mathcal{I}}_\mu) = \begin{cases} \dfrac{\mu_1}{2} I_{1\mu} + \dfrac{\mu_2}{2} I_{2\mu} + \dfrac{1}{2\varepsilon J_\mu} I_{5\mu} \,, & \boldsymbol{X}_\mu \in \mathcal{B}_{0_\mu}^{\mathrm{mat.}} \\[2mm] f_m \Big(\dfrac{\mu_1}{2} I_{1\mu} + \dfrac{\mu_2}{2} I_{2\mu} \Big) + \dfrac{1}{2 f_e \varepsilon J_\mu} I_{5\mu} \,, & \boldsymbol{X}_\mu \in \mathcal{B}_{0_\mu}^{\mathrm{incl.}} \end{cases} ,$$

$$\mathcal{P}_{\mathrm{vol}\mu}(\boldsymbol{X}_\mu, J_\mu) = \begin{cases} -\dfrac{\mu_1 + 2\mu_2}{2} \log(J_\mu) + \dfrac{\lambda}{2} (J_\mu - 1)^2 \,, & \boldsymbol{X}_\mu \in \mathcal{B}_{0_\mu}^{\mathrm{mat.}} \\[2mm] f_m \Big(-\dfrac{\mu_1 + 2\mu_2}{2} \log(J_\mu) + \dfrac{\lambda}{2} (J_\mu - 1)^2 \Big) \,, & \boldsymbol{X}_\mu \in \mathcal{B}_{0_\mu}^{\mathrm{incl.}} \end{cases} . \tag{59}$$

Here, $\mathcal{B}_{0_\mu}^{\mathrm{mat.}}$ and $\mathcal{B}_{0_\mu}^{\mathrm{incl.}}$ denote the subdomains of $\mathcal{B}_{0_\mu}$ corresponding to the matrix and the spherical inclusion, respectively, see Fig. 8. Clearly, both matrix and inclusion constituents are described by means of isotropic internal energy densities. Furthermore, f_m, f_e represent the mechanical and electro-mechanical contrast parameters relating the material properties of both matrix and inclusion. Specifically, we have made use of the following definition for the material parameters

$$\mu_2 = \mu_1 \,, \qquad \lambda = 30\mu_1 \,, \qquad f_m = 2 \,, \qquad f_e = 5 \,. \tag{60}$$

Note that the scaling procedure described in Appendix A with respect to the material parameters μ_1, ε is carried out in order to facilitate the calibration of the ANN based constitutive model, reducing the significant dissimilarity between mechanical and electro-mechanical parameters.
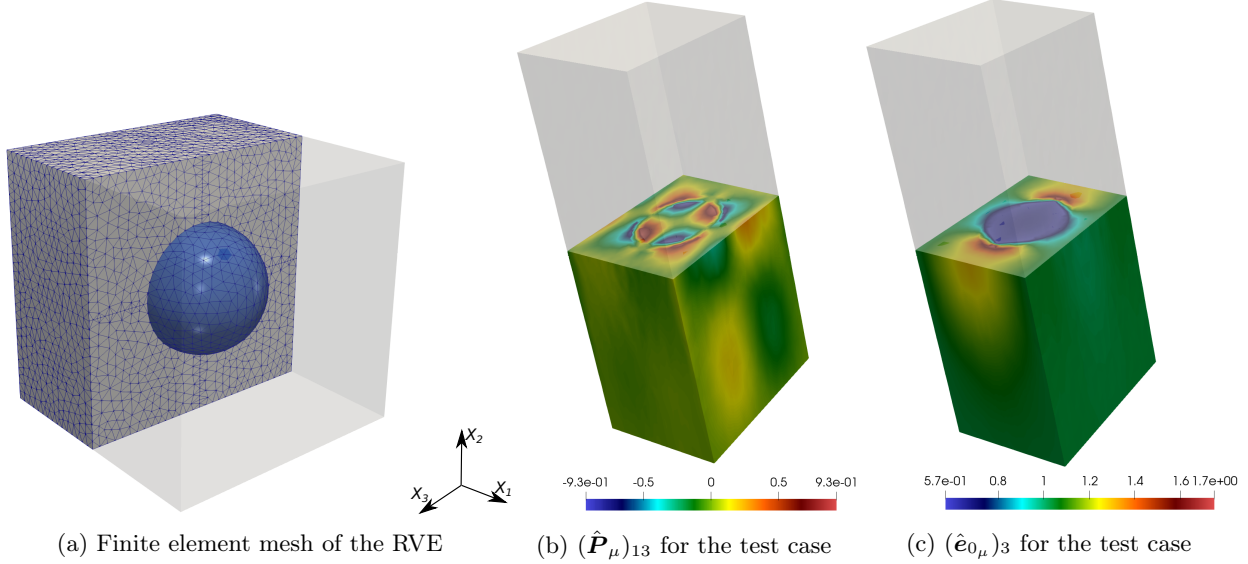
(a) Finite element mesh of the RVE   (b) $(\hat{\boldsymbol{P}}_\mu)_{13}$ for the test case   (c) $(\hat{\boldsymbol{e}}_{0_\mu})_3$ for the test case

Figure 9: Microstructure simulation of the cubic metamaterial. (a) For the the numerical homogenization, the RVE is discretized with quadratic tetrahedral finite elements. (b) and (c) show the highly deformed RVE for the test case at load step 1, i.e., for $\boldsymbol{F}_{11} = 0.5, (\hat{d}_0)_3 = 2$.

For the data generation, the following 6 load cases for the macroscopic fields $\boldsymbol{F}$ and $\boldsymbol{d}_0$ are considered: (1) purely mechanical uniaxial tension, (2) purely mechanical simple shear, (3) the minimum mechanical value for uniaxial tension, with an electric displacement field applied in the X_3-direction, (4) the maximum mechanical value for uniaxial tension, with an electric displacement field applied in the X_3-direction, (5) the minimum mechanical value for shear load, with an electric displacement field applied in the X_1-direction, and (6) and the maximum mechanical value for shear load, with an electric displacement field applied in the X_1-direction. With each single load case consisting of 100 data points, this results in an overall calibration dataset size of 600 data points. In addition, a complex test case is generated, which is illustrated in Figs. 9 and 10.

The finite element discretization of the RVE geometry in Fig. 8, used in order obtain solution of the micro-fluctuation fields (refer to Appendix D) is shown in Fig. 9(a). While Fig. 10 shows the load paths and evaluation of the test case, which will be discussed in detail below in Section 6.3, Figs. 9b and 9c visualize the deformed state at load step 1, i.e., for $\boldsymbol{F}_{11} = 0.5, (\hat{d}_0)_3 = 2$ (see Appendix A for the definition of the scaled fields). Specifically, the microscopic (scaled) first Piola-Kirchhoff stress tensor $(\hat{\boldsymbol{P}}_\mu)_{13}$ and the microscopic (scaled) electric field $(\hat{\boldsymbol{e}}_{0_\mu})_3$ are visualized over half of the RVE in its deformed configuration. For both stress and electric field, highly varying patterns can be observed, which illustrates the complexity of the behavior of the microstructure.

6.2 Model calibration

For the invariant-based ANN model proposed in Section 3, we use the input

$$\boldsymbol{\mathcal{I}} = \left(I_1, \ I_2, \ J, \ -J, \ \hat{I}_4, \ \hat{I}_5, \ J_1^{\mathrm{cub}}, \ J_2^{\mathrm{cub}}, \ \hat{J}_3^{\mathrm{cub}} \right) \in \mathbb{R}^9 \,, \tag{61}$$

with the invariants as described in Section 2.2 and the scaling as described in Appendix A. Again, we choose two ICNN network architectures: one consisting of only one hidden layer with 8 nodes ($H = 1, n^{[1]} = 8$) and one consisting of two hidden layers with 16 nodes in each layer ($H = 2, n^{[h]} = 16$), for which we use the short notations $\mathcal{SP}^+(\boldsymbol{\mathcal{I}}; 8)$ and $\mathcal{SP}^+(\boldsymbol{\mathcal{I}}; 16, 16)$, respectively. The former has

25

Architecture	$\log_{10}$ MSE	
	calibration	test
$\mathcal{SP}^+(\boldsymbol{\mathcal{I}}; 8)$	-3.98	-2.82
—"—	-4.02	-2.74
—"—	-3.97	-2.72
$\mathcal{SP}^+(\boldsymbol{\mathcal{I}}; 16, 16)$	-4.10	-2.76
—"—	-4.12	-2.76
—"—	-4.07	-2.70

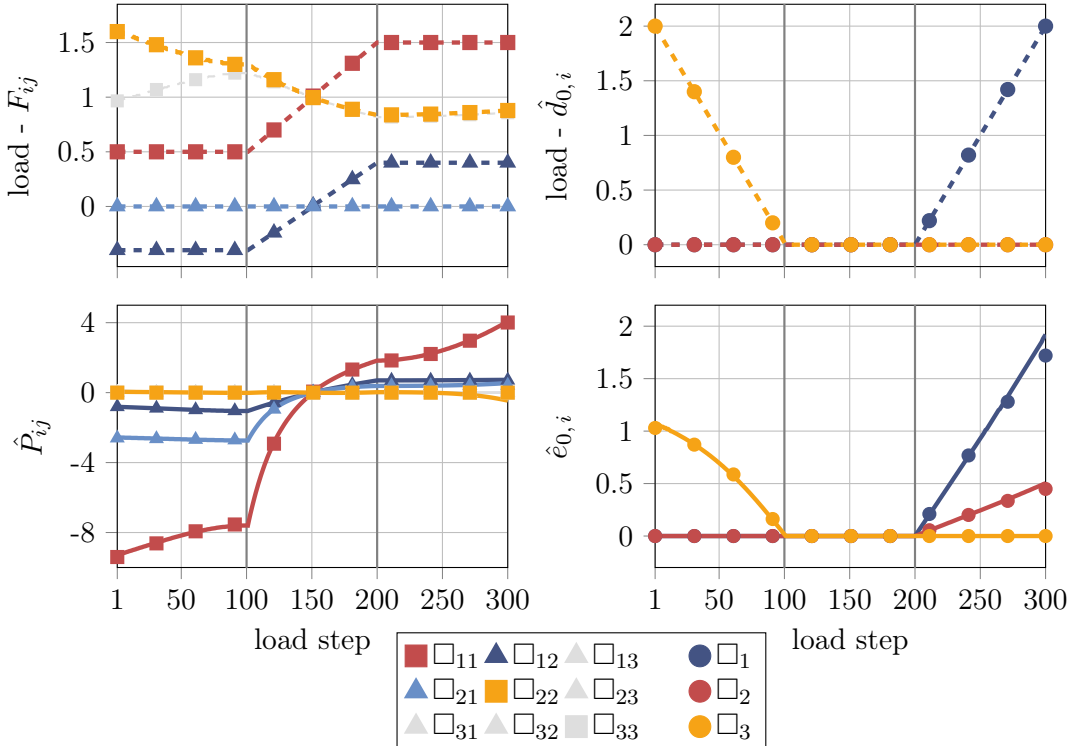Table 2: MSEs of the calibrated ANN based models for the cubic metamaterial

Figure 10: Evaluation of the test case for the cubic metamaterial. Points depict homogenization data, while lines depict the evaluation of the ANN based models. All quantities are dimensionless.

a total amount of 89 free parameters, the latter has 449 free parameters. Each model architecture was initialized three times, using different randomly initialized model parameters each time. The calibration is carried out for 2,500 epochs. The full batch of training data is used with TensorFlow's default learning rate and default batch size. For the remaining calibration details, see Section 4.2.

6.3 Model evaluation

In Table 2, the MSEs of the different model initializations are provided. Both architectures show excellent results for the calibration dataset with slightly worse MSEs for the test dataset. Overall, the model with the smaller network architecture is sufficiently flexible and using a bigger architecture does not improve the results.

In Fig. 10, the evaluation of the test case is shown. For the load steps 101 to 200, the load is purely

mechanical, with a deformation gradient consisting of both normal and shear components, thus representing a general deformation state. For both the minimum and the maximum of the applied deformation gradient, an additional electric displacement field is applied in different directions in load steps 1 to 100 and 201 to 300, respectively. The prediction of the model for the stress tensor is excellent, both for purely mechanical and electro-mechanical load cases. Also, the prediction of the electrical field is excellent, with only slight visible deviations.

Once again, this example demonstrates how the physics-augmented neural network constitutive model is able to represent the coupling between electrical and mechanical effects, and furthermore shows the straightforward applicability to arbitrary symmetry groups.

7   Conclusion

In the present work, a machine learning based constitutive model for reversible electro-mechanically coupled material behavior at finite deformations is proposed. Using different sets of invariants as inputs, an electro-elastic internal energy density is formulated as a convex neural network. In this way, the model fulfills the polyconvexity condition which ensures material stability, as well as thermodynamic consistency, objectivity, material symmetry, and growth conditions. Depending on the considered invariants, this physics-augmented machine learning model can either be applied for compressible or nearly incompressible material behavior, as well as for arbitrary material symmetry classes.

In Section 4, the model is calibrated to data generated with an analytical potential, where the input space $\boldsymbol{F} \in \mathrm{GL}^+(3)$, $\boldsymbol{d}_0 \in \mathbb{R}^3$ is sampled using an algorithm proposed by Kunc and Fritzen [52]. Using this example, the trade-off between structure and flexibility is discussed, which is inherent to constitutive modeling. First of all, including constitutive requirements in the model formulation leads to reliable, i.e., physically sensible model predictions. This can be achieved, for example, by using invariants. But more than that, including constitutive requirements provides the model a pronounced mathematical structure, which helps to generalize with moderate amounts of data. This is especially important for neural networks, which would otherwise require a large amount of data for the calibration. In that sense, constitutive conditions can be seen as an *inductive bias* [33]. On the other side, including constitutive requirements possibly leads to a loss of flexibility, e.g., when for a given anisotropy no complete basis in (polyconvex) invariants can be constructed. However, the restrictions made in this work are either physically well based, e.g., the use of an internal energy which ensures the second law of thermodynamics, or they have a strong mathematical motivation, such as the polyconvexity condition which ensures material stability. Therefore, they should not be seen as strong assumptions on the model behavior, rather they lead to reliable model predictions, while also improving the generalization properties of the model.

The applicability and versatility of this physics-augmented neural network constitutive model is demonstrated by calibrating it to two more datasets. In Section 5, the model is applied for the effective constitutive modeling of an analytically homogenized, transversely isotropic rank-one laminate. In Section 6, a cubic metamaterial is numerically homogenized, and the generated data is then used to calibrate the effective material model. In both cases, the calibration datasets have a fairly small size, and the model predictions are excellent. This shows both the excellent flexibility of the model, which is required to capture the complex behavior of electro-mechanically coupled microstructures, as well as the straightforward applicability towards arbitrary symmetry groups.

Considering the infinitely continuously differentiable neural network cores and the capability of automatic differentiation, an implementation of the proposed model into a finite element framework

will be straightforward, c.f. [43]. With the material stability condition fulfilled by construction, it can be expected to have a favorable numerical behavior, c.f. [3]. Thus, in future work we aim to apply the physics-augmented machine learning models for macroscopic finite element simulations of nonlinear EAP composites and metamaterials. Furthermore, due to the similar mathematical structure, the extension of the model towards electro-magneto-mechanically coupled material behavior [12] should be relatively straightforward.

Data availability. The authors provide access to the simulation data required to reproduce the results through the public GitHub repository `https://github.com/CPShub/sim-data`.

Appendix

A Scaling of internal energy density functions

This section describes the scaling procedure used in this work for the definition of the various internal energy functions used throughout Sections 4, 5 and 6. This procedure will be initially described and particularized for the analytical transversely isotropic potential shown in Section 4, and generalized afterwards to the other two cases addressed in Sections 5 and 6.

Transversely isotropic model. Typically, in an electro-mechanical constitutive model such as the one defined in Eq. (47), the difference between the mechanical parameters $\mu_1, \mu_2, \mu_3, \lambda$ and the electrical parameters $\varepsilon_1, \varepsilon_2$ is of several orders of magnitude. This scaling difference can entail numerical difficulties for the construction and calibration of a suitable neural network capturing both underlying physics, namely mechanical and electro-mechanical. With the aim of circumventing this potential drawback, for the particular model in Eq. (47) we define the scaled internal energy density $\hat{e}^{\mathrm{ti}}(\boldsymbol{F}, \hat{\boldsymbol{d}}_0)$, in terms of the scaled electric displacement field $\hat{\boldsymbol{d}}_0$, as

$$\hat{e}^{\mathrm{ti}}(\hat{\boldsymbol{\mathcal{U}}}) = \hat{e}^{\mathrm{ti}}(\boldsymbol{F}, \hat{\boldsymbol{d}}_0) = \frac{1}{\mu_1} e(\boldsymbol{F}, \boldsymbol{d}_0) \qquad \text{with} \qquad \hat{\boldsymbol{d}}_0 = \frac{\boldsymbol{d}_0}{\sqrt{\mu_1 \varepsilon_1}}, \quad \hat{\boldsymbol{\mathcal{U}}} = \left\{ \boldsymbol{F}, \hat{\boldsymbol{d}}_0 \right\}. \qquad (A.1)$$

Note that the components of $\boldsymbol{F}$ are dimensionless and $\mathcal{O}(1)$, thus $\boldsymbol{F}$ does not need to be scaled.

The scaled internal energy in Eq. (A.1) admits the same additive decomposition as in Eq. (46), namely

$$\hat{e}^{\mathrm{ti}}(\hat{\boldsymbol{\mathcal{U}}}) = \hat{\mathcal{P}}(\hat{\boldsymbol{\mathcal{V}}}) = \hat{\tilde{\mathcal{P}}}(\hat{\tilde{\boldsymbol{\mathcal{I}}}}^{\mathrm{iso}}) + \hat{\tilde{\mathcal{P}}}(\hat{\boldsymbol{\mathcal{J}}}^{\mathrm{ti}}) + \hat{e}_{\mathrm{vol}}(J), \qquad (A.2)$$

where $\hat{\boldsymbol{\mathcal{V}}} = \{\boldsymbol{F}, \boldsymbol{H}, J, \hat{\boldsymbol{d}}_0, \hat{\boldsymbol{d}}\}$ with $\hat{\boldsymbol{d}} = \boldsymbol{F}\hat{\boldsymbol{d}}_0$. Each scaled contribution is defined as

$$\hat{\tilde{\mathcal{P}}}(\hat{\tilde{\boldsymbol{\mathcal{I}}}}^{\text{iso}}) = \frac{\bar{I}_1}{2} + \frac{\mu_2}{2\mu_1}\bar{I}_2 - \frac{\mu_3}{\mu_1}\log J + \frac{\hat{I}_5}{2J},$$

$$\hat{\tilde{\mathcal{P}}}(\hat{\boldsymbol{\mathcal{J}}}^{\text{ti}}) = \frac{\mu_3}{2\mu_1}\left(\frac{(J_1^{\text{ti}})^{a_1}}{a_1} + \frac{(J_2^{\text{ti}})^{a_2}}{a_2}\right) + \frac{\varepsilon_1}{2\varepsilon_2}\hat{J}_3^{\text{ti}}, \tag{A.3}$$

$$\hat{e}_{\text{vol}}(J) = \frac{\lambda}{2\mu_1}(J-1)^2,$$

where $\hat{\tilde{\boldsymbol{\mathcal{I}}}}^{\text{iso}}$ and $\hat{\boldsymbol{\mathcal{J}}}^{\text{ti}}$ are comprised of scaled (dimensionless) invariants,

$$\hat{\tilde{\boldsymbol{\mathcal{I}}}}^{\text{iso}} = \{\bar{I}_1, \bar{I}_2, \hat{I}_4, \hat{I}_5, J\}, \qquad \hat{\boldsymbol{\mathcal{J}}}^{\text{ti}} = \{J_1^{\text{ti}}, J_2^{\text{ti}}, \hat{J}_3^{\text{ti}}\}, \tag{A.4}$$

with the new scaled invariants $\{\hat{I}_4, \hat{I}_5, \hat{J}_3^{\text{ti}}, \hat{J}_4^{\text{ti}}\}$ defined as

$$\hat{I}_4 = \|\hat{\boldsymbol{d}}_0\|^2, \qquad \hat{I}_5 = \|\hat{\boldsymbol{d}}\|^2, \qquad \hat{J}_3^{\text{ti}} = \text{tr}\left(\left(\hat{\boldsymbol{d}}_0 \otimes \hat{\boldsymbol{d}}_0\right)\boldsymbol{G}^{\text{ti}}\right), \qquad \hat{J}_4^{\text{ti}} = \text{tr}\left(\left(\hat{\boldsymbol{d}} \otimes \hat{\boldsymbol{d}}\right)\boldsymbol{G}^{\text{ti}}\right). \tag{A.5}$$

The scaled (dimensionless) material electric field $\hat{\boldsymbol{e}}_0$ and the true material electric field $\boldsymbol{e}_0$ can be obtained from their respective associated energy densities according to Eq. (5), i.e.

$$\hat{\boldsymbol{e}}_0 := \frac{\partial \hat{e}(\boldsymbol{F}, \hat{\boldsymbol{d}}_0)}{\partial \hat{\boldsymbol{d}}_0}, \qquad \boldsymbol{e}_0 := \frac{\partial e(\boldsymbol{F}, \boldsymbol{d}_0)}{\partial \boldsymbol{d}_0}, \tag{A.6}$$

which, making use of Eq. (A.1), permits to establish the relationship between both fields as

$$\hat{\boldsymbol{e}}_0 = \sqrt{\frac{\mu_1}{\varepsilon_1}}\boldsymbol{e}_0. \tag{A.7}$$

Similarly, the scaled (dimensionless) first Piola-Kirchhoff stress tensor $\hat{\boldsymbol{P}}$ and the true counterpart $\boldsymbol{P}$ can be obtained from their respective associated energy densities according to Eq. (5), i.e.

$$\hat{\boldsymbol{P}} := \frac{\partial \hat{e}(\boldsymbol{F}, \hat{\boldsymbol{d}}_0)}{\partial \boldsymbol{F}}, \qquad \boldsymbol{P} := \frac{\partial e(\boldsymbol{F}, \boldsymbol{d}_0)}{\partial \boldsymbol{F}}, \tag{A.8}$$

which, making use of Eq. (A.1), permits to establish the relationship between both fields as

$$\hat{\boldsymbol{P}} = \frac{1}{\mu_1}\boldsymbol{P}. \tag{A.9}$$

Rank-one laminate. With regard to the internal energies of each of the phases a and b of the rank-one laminate composite described in Section 5, c.f. Eq. (52), we used the following scaled internal energies with respect to the material parameters μ_1 and ε of the phase a, namely

$$\hat{\tilde{\mathcal{P}}}^a(\hat{\boldsymbol{\mathcal{I}}}^a) = \frac{1}{2}I_1^a + \frac{\mu_2}{2\mu_1}I_2^a + \frac{\hat{I}_5^a}{2J^a}, \qquad \hat{\mathcal{P}}_{\text{vol}}^a(J^a) = \frac{\lambda}{2\mu_1}(J^a-1)^2,$$

$$\hat{\tilde{\mathcal{P}}}^b(\hat{\boldsymbol{\mathcal{I}}}^b) = f_m\left(\frac{1}{2}I_1^b + \frac{\mu_2}{2\mu_1}I_2^b\right) + \frac{\hat{I}_5^b}{2f_e J^b}, \qquad \hat{\mathcal{P}}_{\text{vol}}^b(J^b) = f_m\frac{\lambda}{2\mu_1}(J^b-1)^2, \tag{A.10}$$

with

$$\hat{I}_5^{a,b} = \|\hat{\boldsymbol{d}}^{a,b}\|^2, \qquad \hat{\boldsymbol{d}}^{a,b} = \boldsymbol{F}^{a,b}\hat{\boldsymbol{d}}_0^{a,b}, \qquad \hat{\boldsymbol{d}}_0^{a,b} = \frac{\boldsymbol{d}_0^{a,b}}{\sqrt{\mu_1\varepsilon}}. \tag{A.11}$$

Cubic metamaterial. An identical scaling procedure in terms of the parameters μ_1, ε of the matrix, analogous to Eqs. (A.10) and (A.11), is applied to the internal energies of the matrix and inclusion material phases within the RVE of the cubic metamaterial in Section 6.

B Concentric sampling strategy

In order to create data of the global behavior of the analytical potential in Section 4, c.f. Eq. (46), the sampling of the input space $\boldsymbol{F} \in \mathrm{GL}^+(3)$ and $\boldsymbol{d} \in \mathbb{R}^3$ in a wide range is now described. Uniform sampling of $\mathrm{GL}^+(3)$ and $\mathbb{R}^3$ is anything but practical, as it would quickly exceed a reasonable dataset size while possibly containing large deformations, potentially outside a relevant range. Therefore, we choose the sampling strategy proposed by Kunc and Fritzen [52], which is now shortly described.

At first, the polar decomposition $\boldsymbol{F} = \boldsymbol{R}\boldsymbol{U}$ is applied to the deformation gradient, where $\boldsymbol{R} \in \mathrm{SO}(3)$ is the rotation tensor and $\boldsymbol{U}$ is the symmetric positive definite (s.p.d.) right stretch tensor [36, Section 2.6]. The objectivity condition implies that constitutive models must be independent of $\boldsymbol{R}$. Therefore, it is sufficient to sample $\boldsymbol{U}$, on which the isochoric-volumetric decomposition $\boldsymbol{U} = J^{1/3} \bar{\boldsymbol{U}}$ is applied [36, Section 6.4]. In doing so, the volume ratio J of the deformation and the isochoric part of the deformation $\bar{\boldsymbol{U}}$ can be sampled independent of each other. This makes it easier to generate stretch tensors $\boldsymbol{U}$ in a practically relevant range.

As $J \in \mathbb{R}^+$, it is straightforward to sample the volume ratio by choosing sensible values around $J = 1$, depending on the compressibility of the considered material. As we assume nearly incompressible material behavior, we set $J = 1$. For the isochoric part, the unimodular s.p.d. tensor space in which $\bar{\boldsymbol{U}}$ lies has to be sampled. After some Lie group theory, this can be formulated equivalently to sampling a five-dimensional linear space. Altogether, the strategy proposed by Kunc and Fritzen [52] provides a straightforward generation of uniformly distributed stretch tensors $\boldsymbol{U}$. Still, it should be noted that uniformly distributed stretch tensors $\boldsymbol{U}$ may not be optimal, as this approach does not take the material symmetry into account and may yield redundant information. However, as the optimal sampling of deformation spaces for specific symmetry groups is not a straightforward task, we pragmatically use this algorithm. Here, for the data generation in Section 4, we employ 30 deviatoric directions and 50 deviatoric amplitudes between 0.1 and 1 for the sampling of $\boldsymbol{U}$.

The sampling of the scaled electric displacement field $\hat{\boldsymbol{d}}_0$ in the Euclidian vector space $\mathbb{R}^3$ is much more straightforward. Here, we sample by using (nearly) equidistant points on a unit sphere and scaling these unit vectors with different amplitudes. In particular, we use 20 equidistant vectors on a unit sphere, which are scaled by 50 amplitudes between 0 and 4.

Altogether, this results in a fairly large dataset with 1.5 million points. As it is shown in Section 4, such a large dataset is not necessary to calibrate (physics-augmented) machine learning models, however, it is useful to examine some specific model properties.

C Analytical homogenization of rank-one laminated composites

C.1 Preliminaries

Let us consider an electro-active material whose microstructure corresponds to a rank-one laminate composite as introduced in Section 5 and illustrated in Fig. 5, c.f. [59]. Now, the macroscopic deformation gradient $\boldsymbol{F}$ and electric displacement field $\boldsymbol{d}_0$ are defined as the weighted sum of those in each phase, namely

$$\boldsymbol{F} = c^a \boldsymbol{F}^a + c^b \boldsymbol{F}^b, \qquad \boldsymbol{d}_0 = c^a \boldsymbol{d}_0^a + c^b \boldsymbol{d}_0^b, \tag{C.1}$$

where indices a and b are used to indicate the respective microscale phases of the laminate. Strong continuity of the tangential and normal components of $\boldsymbol{F}$ and $\boldsymbol{d}_0$ across the laminate interface entails

$$\llbracket \boldsymbol{F} \rrbracket \times \boldsymbol{l}_0 = \boldsymbol{0}\,, \qquad \llbracket \boldsymbol{d}_0 \rrbracket \cdot \boldsymbol{l}_0 = 0 \qquad \text{with} \qquad \llbracket \bullet \rrbracket = (\bullet)^a - (\bullet)^b\,. \tag{C.2}$$

These conditions can alternatively be written in a more convenient form as

$$\llbracket \boldsymbol{F} \rrbracket = \boldsymbol{\alpha} \otimes \boldsymbol{l}_0\,, \qquad \llbracket \boldsymbol{d}_0 \rrbracket = \boldsymbol{T}_{\boldsymbol{l}_0} \boldsymbol{\beta}\,, \tag{C.3}$$

where $\boldsymbol{\alpha} \in \mathbb{R}^3$ denotes the microscale deformation gradient amplitude vector and $\boldsymbol{\beta} \in \mathbb{R}^2$ the microscale electric displacement amplitude. $\boldsymbol{T}_{\boldsymbol{l}_0} \in \mathbb{R}^{3\times 2}$ is defined as $\boldsymbol{T}_{\boldsymbol{l}_0} = \boldsymbol{t}_{0_1} \otimes \boldsymbol{e}_1^\star + \boldsymbol{t}_{0_2} \otimes \boldsymbol{e}_2^\star$, with $\boldsymbol{t}_{0_1}$ and $\boldsymbol{t}_{0_2}$ being two vectors orthonormal to $\boldsymbol{l}_0$ and to each other, and with the 2D unit vectors $\boldsymbol{e}_1^\star = \begin{pmatrix} 1 & 0 \end{pmatrix}^T$ and $\boldsymbol{e}_2^\star = \begin{pmatrix} 0 & 1 \end{pmatrix}^T$. Combination of Eq. (C.1) and Eq. (C.3) permits to obtain $\boldsymbol{F}^{a,b}$ and $\boldsymbol{d}_0^{a,b}$ as

$$\begin{aligned} \boldsymbol{F}^a(\boldsymbol{F}, \boldsymbol{\alpha}) &= \boldsymbol{F} + c^b \boldsymbol{\alpha} \otimes \boldsymbol{l}_0\,, & \boldsymbol{d}_0^a(\boldsymbol{d}_0, \boldsymbol{\beta}) &= \boldsymbol{d}_0 + c^b \boldsymbol{T}_{\boldsymbol{l}_0} \boldsymbol{\beta}\,, \\ \boldsymbol{F}^b(\boldsymbol{F}, \boldsymbol{\alpha}) &= \boldsymbol{F} - c^a \boldsymbol{\alpha} \otimes \boldsymbol{l}_0\,, & \boldsymbol{d}_0^b(\boldsymbol{d}_0, \boldsymbol{\beta}) &= \boldsymbol{d}_0 - c^a \boldsymbol{T}_{\boldsymbol{l}_0} \boldsymbol{\beta}\,. \end{aligned} \tag{C.4}$$

The homogenized or effective internal energy of the composite $e(\boldsymbol{F}, \boldsymbol{d}_0)$ can be postulated as

$$e\left(\boldsymbol{F}, \boldsymbol{d}_0\right) = \min_{\boldsymbol{\alpha}, \boldsymbol{\beta}} \left\{ e^\star(\boldsymbol{F}, \boldsymbol{d}_0, \boldsymbol{\alpha}, \boldsymbol{\beta}) \right\}\,, \tag{C.5}$$

with

$$e^\star(\boldsymbol{F}, \boldsymbol{d}_0, \boldsymbol{\alpha}, \boldsymbol{\beta}) = c^a e^a \left(\boldsymbol{F}^a\left(\boldsymbol{F}, \boldsymbol{\alpha}\right), \boldsymbol{d}_0^a\left(\boldsymbol{d}_0, \boldsymbol{\beta}\right)\right) + c^b e^b \left(\boldsymbol{F}^b\left(\boldsymbol{F}, \boldsymbol{\alpha}\right), \boldsymbol{d}_0^b\left(\boldsymbol{d}_0, \boldsymbol{\beta}\right)\right)\,, \tag{C.6}$$

where $e^a(\boldsymbol{F}^a, \boldsymbol{d}_0^a)$ and $e^b(\boldsymbol{F}^b, \boldsymbol{d}_0^b)$ are the microscale internal energy functions expressed in terms of their respective microscale fields, c.f. Eq. (52). The stationary conditions of Eq. (C.6) with respect to $\boldsymbol{\alpha}, \boldsymbol{\beta}$ yield

$$\begin{aligned} De^\star[\delta \boldsymbol{\alpha}] = 0 & \qquad \Rightarrow \qquad & \llbracket \boldsymbol{P} \rrbracket \boldsymbol{l}_0 = \boldsymbol{0}\,, \\ De^\star[\delta \boldsymbol{\beta}] = 0 & \qquad \Rightarrow \qquad & \boldsymbol{T}_{\boldsymbol{l}_0}^T \llbracket \boldsymbol{e}_0 \rrbracket = \boldsymbol{0} \qquad \Leftrightarrow \qquad \llbracket \boldsymbol{e}_0 \rrbracket \times \boldsymbol{l}_0 = \boldsymbol{0}\,, \end{aligned} \tag{C.7}$$

which represent the strong enforcement of the normal and tangential components of the traction vector and $\boldsymbol{e}_0$, respectively. Thus, the homogenized energy functional $e(\boldsymbol{F}, \boldsymbol{d}_0)$ can be re-written as

$$e(\boldsymbol{F}, \boldsymbol{d}_0) = e^\star(\boldsymbol{F}, \boldsymbol{d}_0, \boldsymbol{\alpha}, \boldsymbol{\beta})\big|_{\text{s.t. } \{\llbracket \boldsymbol{P} \rrbracket \boldsymbol{l}_0 = \boldsymbol{0},\, \llbracket \boldsymbol{e}_0 \rrbracket \times \boldsymbol{l}_0 = \boldsymbol{0}\}}\,. \tag{C.8}$$

C.2 Solution of amplitude vectors

The stationary conditions Eq. (C.7) represent a system of nonlinear equations, where the microscale amplitude vectors $\boldsymbol{\alpha}, \boldsymbol{\beta}$ can be resolved in terms of the macroscale homogenized fields $\boldsymbol{F}, \boldsymbol{d}_0$. The computation of $\boldsymbol{\alpha}, \boldsymbol{\beta}$ can be carried out with a k-iterative Newton-Raphson algorithm, namely

$$\begin{aligned} \text{Solve} \qquad & De^\star[\delta \boldsymbol{\alpha}, \delta \boldsymbol{\beta}]\Big|^k + D^2 e^\star[\delta \boldsymbol{\alpha}, \delta \boldsymbol{\beta}; \Delta \boldsymbol{\alpha}, \Delta \boldsymbol{\beta}]\Big|^k = \boldsymbol{0} \quad \text{for} \quad \Delta \boldsymbol{\alpha}, \Delta \boldsymbol{\beta}\,, \\ \text{Update} \qquad & \boldsymbol{\alpha}^{k+1} = \boldsymbol{\alpha}^k + \Delta \boldsymbol{\alpha}, \qquad \boldsymbol{\beta}^{k+1} = \boldsymbol{\beta}^k + \Delta \boldsymbol{\beta}\,. \end{aligned} \tag{C.9}$$

In [59] it was shown that Eq. (C.9) can be written as

$$\begin{bmatrix} \Delta \boldsymbol{\alpha} \\ \Delta \boldsymbol{\beta} \end{bmatrix} = - \left[\hat{\mathbb{H}}_e^{\boldsymbol{l}_0} \right]_k^{-1} \begin{bmatrix} \llbracket \boldsymbol{P} \rrbracket \boldsymbol{l}_0 \\ \boldsymbol{T}_{\boldsymbol{l}_0}^T \llbracket \boldsymbol{e}_0 \rrbracket \end{bmatrix}_k\,, \tag{C.10}$$

where the second order tensor $\left[\hat{\mathbb{H}}_e^{l_0} \right]$ is defined as

$$\left[\hat{\mathbb{H}}_e^{l_0} \right] = c^b \begin{bmatrix} \boldsymbol{K}_1^a & \boldsymbol{K}_2^a \\ (\boldsymbol{K}_2^a)^T & \boldsymbol{K}_3^a \end{bmatrix} + c^a \begin{bmatrix} \boldsymbol{K}_1^b & \boldsymbol{K}_2^b \\ (\boldsymbol{K}_2^b)^T & \boldsymbol{K}_3^b \end{bmatrix}, \tag{C.11}$$

where the individual sub-matrices are defined as

$$\left(\boldsymbol{K}_1^{a,b} \right)_{ij} = \left(\frac{\partial^2 e^{a,b}}{\partial \boldsymbol{F}^{a,b} \partial \boldsymbol{F}^{a,b}} \right)_{iPjQ} (\boldsymbol{l}_0)_P (\boldsymbol{l}_0)_Q, \qquad \boldsymbol{K}_3^{a,b} = \boldsymbol{T}_{l_0}^T \frac{\partial^2 e^{a,b}}{\partial \boldsymbol{F}^{a,b} \partial \boldsymbol{d}_0^{a,b}} \boldsymbol{T}_{l_0},$$

$$\left(\boldsymbol{K}_2^{a,b} \right)_{iJ} = (\boldsymbol{l}_0)_P \left(\frac{\partial^2 e^{a,b}}{\partial \boldsymbol{F}^{a,b} \partial \boldsymbol{d}_0^{a,b}} \right)_{iPQ} (\boldsymbol{T}_{l_0})_{QJ}. \tag{C.12}$$

To ensure the existence of solutions of Eq. (C.10), and hence for $\boldsymbol{\alpha}, \boldsymbol{\beta}$, the second directional derivative of $e^\star$ with respect to $\{\boldsymbol{\alpha}, \boldsymbol{\beta}\}$ must be (strictly) positive definite, namely

$$D^2 e^\star[\delta\boldsymbol{\alpha}, \delta\boldsymbol{\beta}; \delta\boldsymbol{\alpha}, \delta\boldsymbol{\beta}] > 0 \qquad \forall \delta\boldsymbol{\alpha}, \delta\boldsymbol{\beta}, \tag{C.13}$$

Marín et al. [59] showed that $D^2 e^\star[\delta\boldsymbol{\alpha}, \delta\boldsymbol{\beta}; \delta\boldsymbol{\alpha}, \delta\boldsymbol{\beta}]$ is positive provided that both e^a and e^b are elliptic, c.f. see Eq. (10). Thus, provided that e^a and e^b are both polyconvex, above inequality Eq. (C.13) is fulfilled, and thus existence of the solution $\boldsymbol{\alpha}, \boldsymbol{\beta}$ is always guaranteed here.

C.3   Effective stress and electric field

From the internal energy of each phase, namely $e^a(\boldsymbol{F}^a, \boldsymbol{d}_0^a)$ or $e^b(\boldsymbol{F}^b, \boldsymbol{d}_0^b)$, it is possible to obtain the respective first Piola-Kirchhoff stress tensor and electric field according to Eq. (5) as

$$\boldsymbol{P}^a = \frac{\partial e^a(\boldsymbol{\mathcal{U}}^a)}{\partial \boldsymbol{F}^a}, \qquad \boldsymbol{P}^b = \frac{\partial e^b(\boldsymbol{\mathcal{U}}^b)}{\partial \boldsymbol{F}^b}, \qquad \boldsymbol{e}_0^a = \frac{\partial e^a(\boldsymbol{\mathcal{U}}^a)}{\partial \boldsymbol{d}_0^a}, \qquad \boldsymbol{e}_0^b = \frac{\partial e^b(\boldsymbol{\mathcal{U}}^b)}{\partial \boldsymbol{d}_0^b}. \tag{C.14}$$

Differentiation of Eq. (C.8) with respect to time yields the balance of power between macro and micro scales, i.e.

$$\dot{e}(\boldsymbol{F}, \boldsymbol{d}_0) = \dot{e}^\star(\boldsymbol{F}, \boldsymbol{d}_0, \boldsymbol{\alpha}, \boldsymbol{\beta}) \qquad \Rightarrow \qquad \boldsymbol{P} : \dot{\boldsymbol{F}} + \boldsymbol{e}_0 \cdot \dot{\boldsymbol{d}}_0 = De^\star[\dot{\boldsymbol{F}}] + De^\star[\dot{\boldsymbol{d}}_0], \tag{C.15}$$

where the directional derivatives $De^\star[\dot{\boldsymbol{F}}]$ and $De^\star[\dot{\boldsymbol{d}}_0]$ are

$$De^\star[\dot{\boldsymbol{F}}] = \left(c^a \boldsymbol{P}^a + c^b \boldsymbol{P}^b \right) : \dot{\boldsymbol{F}} + \underbrace{c^a c^b D\tilde{\boldsymbol{\alpha}}[\dot{\boldsymbol{F}}] \cdot (\llbracket \boldsymbol{P} \rrbracket \boldsymbol{l}_0)}_{=0} + \underbrace{c^a c^b D\tilde{\boldsymbol{\beta}}[\dot{\boldsymbol{F}}] \cdot \left(\boldsymbol{T}_{l_0}^T \llbracket \boldsymbol{e}_0 \rrbracket \right)}_{=0},$$

$$De^\star[\dot{\boldsymbol{d}}_0] = \left(c^a \boldsymbol{e}_0^a + c^b \boldsymbol{e}_0^b \right) \cdot \dot{\boldsymbol{d}}_0 + \underbrace{c^a c^b D\tilde{\boldsymbol{\alpha}}[\dot{\boldsymbol{d}}_0] \cdot (\llbracket \boldsymbol{P} \rrbracket \boldsymbol{l}_0)}_{=0} + \underbrace{c^a c^b D\tilde{\boldsymbol{\beta}}[\dot{\boldsymbol{d}}_0] \cdot \left(\boldsymbol{\mathcal{T}}_{l_0}^T \llbracket \boldsymbol{e}_0 \rrbracket \right)}_{=0}, \tag{C.16}$$

where use of Eq. (C.14) has been made. Use of Eq. (C.7) enables the last two contributions in Eq. (C.16) to vanish. Then, introduction of Eq. (C.16) into Eq. (C.15) permits to obtain the Hill-Mandel principle in the context of electro-mechanics, particularized to the case of rank-one laminate composites, i.e.

$$\boldsymbol{P} : \dot{\boldsymbol{F}} + \boldsymbol{e}_0 \cdot \dot{\boldsymbol{d}}_0 = \left(c^a \boldsymbol{P}^a + c^b \boldsymbol{P}^b \right) : \dot{\boldsymbol{F}} + \left(c^a \boldsymbol{e}_0^a + c^b \boldsymbol{e}_0^b \right) \cdot \dot{\boldsymbol{d}}_0. \tag{C.17}$$

From this Hill-Mandel principle, it is possible to obtain the relationship between the macroscopic fields $\boldsymbol{P}, \boldsymbol{e}_0$ and their microscopic counterparts $\boldsymbol{P}^a, \boldsymbol{P}^b$ and $\boldsymbol{e}_0^a, \boldsymbol{e}_0^b$, as

$$\boldsymbol{P} = c^a \boldsymbol{P}^a + c^b \boldsymbol{P}^b, \qquad \boldsymbol{e}_0 = c^a \boldsymbol{e}_0^a + c^b \boldsymbol{e}_0^b. \tag{C.18}$$

32

D Numerical homogenization of the cubic metamaterial

D.1 Preliminaries

For the case of an electro-active material whose microstructure corresponds to the cubic metamaterial as introduced in Section 6 and illustrated in Fig. 8, the microscopic fields $\boldsymbol{F}_\mu$ and $\boldsymbol{e}_{0_\mu}$ are defined in terms of the microscopic current position $\boldsymbol{x}_\mu$ and electric potential φ_μ fields as

$$\boldsymbol{F}_\mu = \frac{\partial \boldsymbol{x}_\mu}{\partial \boldsymbol{X}_\mu}, \qquad \boldsymbol{e}_{0_\mu} = -\frac{\partial \varphi_\mu}{\partial \boldsymbol{X}_\mu}. \tag{D.1}$$

In the context of periodic first-order homogenization, c.f. [62], $\boldsymbol{x}_\mu$ and φ_μ can be decomposed into macroscopic and microscopic contributions

$$\boldsymbol{x}_\mu = \widetilde{\boldsymbol{x}}_\mu + \boldsymbol{F}\boldsymbol{X}_\mu, \qquad \varphi_\mu = \widetilde{\varphi}_\mu - \boldsymbol{e}_0 \cdot \boldsymbol{X}_\mu, \tag{D.2}$$

where $\widetilde{\boldsymbol{x}}_\mu : \mathcal{B}_{0_\mu} \to \mathbb{R}^3$ and $\widetilde{\varphi}_\mu : \mathcal{B}_{0_\mu} \to \mathbb{R}$ represent the microscopic fluctuations. The latter are subjected to periodic boundary conditions of the form $[\![\widetilde{\boldsymbol{x}}_\mu]\!] = \boldsymbol{0}$ and $[\![\widetilde{\varphi}_\mu]\!] = 0$, where $[\![(\cdot)]\!] = (\cdot)^+ - (\cdot)^-$ represents the jump of the field $(\cdot)$ across opposite boundaries of $\mathcal{B}_{0_\mu}$. The microscopic fields $\boldsymbol{F}_\mu$ and $\boldsymbol{e}_{0_\mu}$ can be related with their macroscopic counterparts $\boldsymbol{F}$ and $\boldsymbol{e}_0$ as

$$\boldsymbol{F} = \frac{1}{V_\mu} \int_{\mathcal{B}_{0_\mu}} \boldsymbol{F}_\mu(\boldsymbol{X}_\mu)\, dV_\mu = \frac{1}{V_\mu} \int_{\partial \mathcal{B}_{0_\mu}} \boldsymbol{x}_\mu(\boldsymbol{X}_\mu) \otimes \boldsymbol{n}_{0_\mu}(\boldsymbol{X}_\mu)\, dV_\mu,$$

$$\boldsymbol{e}_0 = \frac{1}{V_\mu} \int_{\mathcal{B}_{0_\mu}} \boldsymbol{e}_{0_\mu}(\boldsymbol{X}_\mu)\, dV_\mu = \frac{1}{V_\mu} \int_{\partial \mathcal{B}_{0_\mu}} \varphi_\mu(\boldsymbol{X}_\mu)\, \boldsymbol{n}_{0_\mu}(\boldsymbol{X}_\mu)\, dV_\mu. \tag{D.3}$$

We assume the existence of a Helmholtz type energy density at both macro and microscales, denoted as $\Psi(\boldsymbol{F}, \boldsymbol{e}_0)$ and $\Psi_\mu\left(\boldsymbol{F}_\mu, \boldsymbol{e}_{0_\mu}\right)$, respectively. Then, the effective or macroscopic Helmholtz free energy density is postulated as

$$\underbrace{\Psi(\boldsymbol{F}, \boldsymbol{e}_0) V_\mu}_{\Pi(\widetilde{\boldsymbol{x}}_\mu, \widetilde{\varphi}_\mu)} = \inf_{\widetilde{\boldsymbol{x}}_\mu \in \mathbb{V}^x} \sup_{\widetilde{\varphi}_\mu \in \mathbb{V}^\varphi} \left\{ \int_{\mathcal{B}_{0_\mu}} \Psi_\mu\left(\boldsymbol{F}_\mu, \boldsymbol{e}_{0_\mu}\right)\, dV_\mu \right\}, \tag{D.4}$$

where the relevant functional spaces $\mathbb{V}^x$ and $\mathbb{V}^\varphi$ are

$$\mathbb{V}^x = \left\{ \widetilde{\boldsymbol{x}}_\mu : (\widetilde{\boldsymbol{x}}_\mu)_i \in H_0^1(\mathcal{B}_{0_\mu}), \quad [\![\widetilde{\boldsymbol{x}}_\mu]\!] = \boldsymbol{0},\ \widetilde{\boldsymbol{x}}_\mu = \boldsymbol{0} \text{ on } \partial\mathcal{B}_{0_\mu}^x \right\},$$

$$\mathbb{V}^\varphi = \left\{ \widetilde{\varphi}_\mu : \widetilde{\varphi}_\mu \in H_0^1(\mathcal{B}_{0_\mu}), \qquad [\![\widetilde{\varphi}_\mu]\!] = 0,\ \widetilde{\varphi}_\mu = 0 \text{ on } \partial\mathcal{B}_{0_\mu}^\varphi \right\}, \tag{D.5}$$

where $\partial\mathcal{B}_{0_\mu}^x \subset \partial\mathcal{B}_{0_\mu}$ is the region where zero Dirichlet boundary conditions are prescribed for $\widetilde{\boldsymbol{x}}_\mu$, preventing rigid body motions. Furthermore, $\partial\mathcal{B}_{0_\mu}^\varphi \subset \partial\mathcal{B}_{0_\mu}$ is the region where zero Dirichlet boundary conditions are prescribed for $\widetilde{\varphi}_\mu$, with excluding non-unique solutions of the form $\widetilde{\varphi}_\mu + C,\ \forall C \in \mathbb{R}$.

D.2 Solution of micro-fluctuations

The stationary conditions of the homogenized energy in Eq. (D.4) yields

$$D\Pi(\widetilde{\boldsymbol{x}}_\mu, \widetilde{\varphi}_\mu)[\boldsymbol{v}_x] = \int_{\mathcal{B}_{0_\mu}} \boldsymbol{P}_\mu : \frac{\partial \boldsymbol{v}_x}{\partial \boldsymbol{X}_\mu}\, dV_\mu = 0, \qquad D\Pi(\widetilde{\boldsymbol{x}}_\mu, \widetilde{\varphi}_\mu)[v_\varphi] = -\int_{\mathcal{B}_{0_\mu}} \boldsymbol{d}_{0_\mu} \cdot \frac{\partial v_\varphi}{\partial \boldsymbol{X}_\mu}\, dV_\mu = 0,$$

$$\tag{D.6}$$

which permit to obtain the micro-fluctuations $\widetilde{\boldsymbol{x}}_\mu$ and $\widetilde{\varphi}_\mu$.

In Eq. (D.6), both $\boldsymbol{P}_\mu$ and $\boldsymbol{d}_{0_\mu}$ could in principle be obtained through the following relationships

$$\boldsymbol{P}_\mu = \frac{\partial \Psi_\mu(\boldsymbol{F}_\mu, \boldsymbol{e}_{0_\mu})}{\partial \boldsymbol{F}_\mu}, \qquad \boldsymbol{d}_{0_\mu} = -\frac{\partial \Psi_\mu(\boldsymbol{F}_\mu, \boldsymbol{e}_{0_\mu})}{\partial \boldsymbol{e}_{0_\mu}}. \tag{D.7}$$

However, we advocate for constitutive models which are defined in terms of the microscopic internal energy $e_\mu(\boldsymbol{F}_\mu, \boldsymbol{d}_{0_\mu})$ instead of the Helmholtz free energy $\Psi_\mu(\boldsymbol{F}_\mu, \boldsymbol{e}_{0_\mu})$. Specifically, we consider internal energy densities $e_\mu(\boldsymbol{F}_\mu, \boldsymbol{d}_{0_\mu})$ complying with the polyconvexity condition in Eqs. (6) and (8), namely

$$e_\mu(\boldsymbol{F}_\mu, \boldsymbol{d}_{0_\mu}) = \mathcal{P}_\mu(\boldsymbol{\mathcal{V}}_\mu) \qquad \text{with} \qquad \boldsymbol{\mathcal{V}}_\mu = \{\boldsymbol{F}_\mu, \boldsymbol{H}_\mu, J_\mu, \boldsymbol{d}_{0_\mu}, \boldsymbol{d}_\mu\}, \quad \boldsymbol{d}_\mu = \boldsymbol{F}_\mu \boldsymbol{d}_{0_\mu}, \tag{D.8}$$

where the microscopic fields $\boldsymbol{H}_\mu$ and J_μ are defined in terms of $\boldsymbol{F}_\mu$ as in Eq. (2). As described in Remark 2.2, polyconvexity of the microscopic internal energy density $e_\mu\left(\boldsymbol{F}_\mu, \boldsymbol{d}_{0_\mu}\right)$ guarantees the definition of the microscopic Helmholtz energy density $\Psi_\mu(\boldsymbol{F}_\mu, \boldsymbol{e}_{0_\mu})$ according to the Legendre transformation

$$\Psi_\mu(\boldsymbol{F}_\mu, \boldsymbol{e}_{0_\mu}) = -\sup_{\boldsymbol{d}_{0_\mu}} \left\{ \boldsymbol{e}_{0_\mu} \cdot \boldsymbol{d}_{0_\mu} - e_\mu(\boldsymbol{F}_\mu, \boldsymbol{d}_{0_\mu}) \right\}. \tag{D.9}$$

Given the microscopic fields $\boldsymbol{F}_\mu, \boldsymbol{e}_{0_\mu}$, it is possible to obtain $\boldsymbol{P}_\mu$ and $\boldsymbol{d}_{0_\mu}$ from the (nonlinear) stationary condition of the Legendre transformation in Eq. (D.9) as

$$\boldsymbol{P}_\mu = \frac{\partial e_\mu(\boldsymbol{F}_\mu, \boldsymbol{d}_{0_\mu})}{\partial \boldsymbol{F}_\mu}, \qquad \boldsymbol{e}_{0_\mu} = \frac{\partial e_\mu(\boldsymbol{F}_\mu, \boldsymbol{d}_{0_\mu})}{\partial \boldsymbol{d}_{0_\mu}}. \tag{D.10}$$

Generally, the boundary value problem defined by Eq. (D.6) can only be solved numerically for given macro $\boldsymbol{F}, \boldsymbol{d}_0$, e.g., by discretizing the microscale RVE $\mathcal{B}_{0_\mu}$ and the sought fields $\widetilde{\boldsymbol{x}}_\mu$ and $\widetilde{\varphi}_\mu$ using finite element methods [27, 68]. As mentioned in Section 6.1 and illustrated in Fig. 9a, here we employ tetrahedral elements with quadratic shape functions for both $\widetilde{\boldsymbol{x}}_\mu$ and $\widetilde{\varphi}_\mu$. Since the problem is nonlinear, similar to Appendix C.2, an iterative solution procedure in terms of a Newton-Raphson method is required.

D.3 Effective stress and electric displacement fields

Differentiation with respect to time in above Eq. (D.4) and making use of Eqs. (D.2) and (D.7) yields the following power balance between macro and micro scales,

$$\left(\boldsymbol{P} : \dot{\boldsymbol{F}} - \boldsymbol{d}_0 \cdot \dot{\boldsymbol{e}}_0\right) V_\mu = \int_{\mathcal{B}_{0_\mu}} \boldsymbol{P}_\mu : \left(\frac{\partial \dot{\widetilde{\boldsymbol{x}}}_\mu}{\partial \boldsymbol{X}_{0_\mu}} + \dot{\boldsymbol{F}}\right) - \boldsymbol{d}_{0_\mu} \cdot \left(-\frac{\partial \dot{\widetilde{\varphi}}_\mu}{\partial \boldsymbol{X}_\mu} + \dot{\boldsymbol{e}}_0\right) dV_\mu. \tag{D.11}$$

For $\frac{\partial \dot{\widetilde{\boldsymbol{x}}}_\mu}{\partial \boldsymbol{X}_{0_\mu}} \in \mathbb{V}^x$ and $\frac{\partial \dot{\widetilde{\varphi}}_\mu}{\partial \boldsymbol{X}_\mu} \in \mathbb{V}^\varphi$, substitution of Eq. (D.6) into (D.11) permits to obtain the Hill-Mandel principle in the context of electro-mechanics, namely

$$\left(\boldsymbol{P} : \dot{\boldsymbol{F}} - \boldsymbol{d}_0 \cdot \dot{\boldsymbol{e}}_0\right) V_\mu = \int_{\mathcal{B}_{0_\mu}} \left(\boldsymbol{P}_\mu : \dot{\boldsymbol{F}} - \boldsymbol{d}_{0_\mu} \cdot \dot{\boldsymbol{e}}_0\right) dV_\mu. \tag{D.12}$$

As a consequence, the following relationships between the macroscopic fields $\boldsymbol{P}, \boldsymbol{d}_0$ and their microscopic counterparts $\boldsymbol{P}_\mu, \boldsymbol{d}_{0_\mu}$ can be established,

$$\boldsymbol{P} = \frac{1}{V_\mu} \int_{\mathcal{B}_{0_\mu}} \boldsymbol{P}_\mu \, dV_\mu, \qquad \boldsymbol{d}_0 = \frac{1}{V_\mu} \int_{\mathcal{B}_{0_\mu}} \boldsymbol{d}_{0_\mu} \, dV_\mu. \tag{D.13}$$

References

[1] C. C. Aggarwal. *Neural Networks and Deep Learning*. 1st ed. Springer International Publishing, 2018.

[2] B. Amos, L. Xu, and J. Z. Kolter. "Input convex neural networks". In: *Proceedings of the 34th International Conference on Machine Learning*. Ed. by D. Precup and Y. W. Teh. Vol. 70. Proceedings of Machine Learning Research. PMLR, 2017, pp. 146–155. arXiv: 1609.07152.

[3] F. As'ad, P. Avery, and C. Farhat. "A mechanics-informed artificial neural network approach in data-driven constitutive modeling". In: *International Journal for Numerical Methods in Engineering* 123.12 (2022), pp. 2738–2759. DOI: 10.1002/nme.6957.

[4] H. Baaser, A. Schobel, W. Michaeli, and U. Masberg. "Comparison of equibiaxial testing devices for parameter calibration of material models". In: *Kautschuk Gummi Kunststoffe* 64 (2011), pp. 20–24.

[5] J. Ball. "Constitutive inequalities and existence theorems in nonlinear elasto-statics". In: *Herriot Watt Symposion: Nonlinear Analysis and Mechanics*. Ed. by R. Knops. Vol. 1. London: Pitman, 1977, pp. 187–241.

[6] J. Ball. "Convexity conditions and existence theorems in nonlinear elasticity". In: *Archive for Rational Mechanics and Analysis* 63.4 (1976), pp. 337–403. DOI: 10.1007/BF00279992.

[7] K. Bertoldi and M. Gei. "Instabilities in multilayered soft dielectrics". In: *Journal of the Mechanics and Physics of Solids* 59.1 (2011), pp. 18–42. DOI: http://dx.doi.org/10.1016/j.jmps.2010.10.001.

[8] P. Betsch, A. Janz, and C. Hesch. "A mixed variational framework for the design of energy–momentum schemes inspired by the structure of polyconvex stored energy functions". In: *Computer Methods in Applied Mechanics and Engineering* 335 (2018), pp. 660–696. DOI: 10.1016/j.cma.2018.01.013.

[9] R. Bustamante, A. Dorfmann, and R. Ogden. "Nonlinear electroelastostatics: A variational framework". In: *Zeitschrift für angewandte Mathematik und Physik* 60.1 (2009), pp. 154–177. DOI: 10.1007/s00033-007-7145-0.

[10] R. Bustamante and J. Merodio. "Constitutive structure in coupled non-linear electro-elasticity: Invariant descriptions and constitutive restrictions". In: *International Journal of Non-Linear Mechanics* 46.10 (2011), pp. 1315 –1323. DOI: 10.1016/j.ijnonlinmec.2011.06.010.

[11] R. Bustamante, M. H. B. M. Shariff, and M. Hossain. "Mathematical formulations for elastic magneto-electrically coupled soft materials at finite strains: Time-independent processes". In: *International Journal of Engineering Science* 159 (2021). DOI: 10.1016/j.ijengsci.2020.103429.

[12] R. Bustamante, M. Shariff, and M. Hossain. "Mathematical formulations for elastic magneto-electrically coupled soft materials at finite strains: Time-independent processes". In: *International Journal of Engineering Science* 159 (2021), p. 103429. DOI: 10.1016/j.ijengsci.2020.103429.

[13] S. Cai, Z. Mao, Z. Wang, M. Yin, and G. E. Karniadakis. "Physics-informed neural networks (PINNs) for fluid mechanics: A review". In: *Acta Mechanica Sinica* 37 (2021), pp. 1727–1738. DOI: 10.1007/s10409-021-01148-1.

[14] P. Carrara, L. De Lorenzis, L. Stainier, and M. Ortiz. "Data-driven fracture mechanics". In: *Computer Methods in Applied Mechanics and Engineering* 372 (2020), p. 113390. DOI: 10.1016/j.cma.2020.113390.

[15] V. Champaney, F. Chinesta, and E. Cueto. "Engineering empowered by physics-based and data-driven hybrid models: A methodological overview". In: *International Journal of Material Forming* 15 (2022). DOI: 10.1007/s12289-022-01678-4.

[16] R. T. Q. Chen, Y. Rubanova, J. Bettencourt, and D. Duvenaud. "Neural ordinary differential equations". In: *Pre-print under review* (2019). arXiv: 1806.07366.

[17] H. De Gersem, A. Galetzka, I. G. Ion, D. Loukrezis, and U. Römer. "Magnetic field simulation with data-driven material modeling". In: *IEEE Transactions on Magnetics* 56.8 (2020), pp. 1–6. DOI: 10.1109/TMAG.2020.3002092.

[18] A. Dorfmann and R. Ogden. "Nonlinear electroelastic deformations". In: *Journal of Elasticity* 82.2 (2006), pp. 99–127. DOI: 10.1007/s10659-005-9028-y.

[19] L. Dorfmann and R. Ogden. "Nonlinear electroelasticity". In: *Acta Mechanica* 174 (2005), pp. 167–183. DOI: 10.1007/s00707-004-0202-2.

[20] V. Ebbing. "Design of Polyconvex Energy Functions for All Anisotropy Classes". PhD thesis. Universität Duisburg-Essen, 2010.

[21] V. Ebbing, J. Schröder, and P. Neff. "Approximation of anisotropic elasticity tensors at the reference state with polyconvex energies". In: *Journal of Archive of Applied Mechanics* 79 (2009), pp. 652–657. DOI: 10.1007/s00419-008-0286-6.

[22] M. Fernández, M. Jamshidian, T. Böhlke, K. Kersting, and O. Weeger. "Anisotropic hyperelastic constitutive models for finite deformations combining material theory and data-driven approaches with application to cubic lattice metamaterials". In: *Computational Mechanics* 67.2 (2021), 653–677. DOI: 10.1007/s00466-020-01954-7.

[23] M. Fernández, F. Fritzen, and O. Weeger. "Material modeling for parametric, anisotropic finite strain hyperelasticity based on machine learning with application in optimization of metamaterials". In: *International Journal for Numerical Methods in Engineering* 123.2 (2022), pp. 577–609. DOI: 10.1002/nme.6869.

[24] M. Flaschel, S. Kumar, and L. De Lorenzis. "Discovering plasticity models without stress data". In: *npj Computational Materials* 8 (2022). DOI: 10.1038/s41524-022-00752-4.

[25] M. Flaschel, S. Kumar, and L. De Lorenzis. "Unsupervised discovery of interpretable hyperelastic constitutive laws". In: *Computer Methods in Applied Mechanics and Engineering* 381 (2021), p. 113852. DOI: 10.1016/j.cma.2021.113852.

[26] A. Galetzka, D. Loukrezis, and H. De Gersem. "Data-driven solvers for strongly nonlinear material response". In: *International Journal for Numerical Methods in Engineering* 122.6 (2021), pp. 1538–1562. DOI: 10.1002/nme.6589.

[27] D. Garcia-Gonzalez, M. Moreno, L. Valencia, A. Arias, and D. Velasco. "Influence of elastomeric matrix and particle volume fraction on the mechanical response of magneto-active polymers". In: *Composites Part B: Engineering* 215 (2021). DOI: 10.1016/j.compositesb.2021.108796.

[28] M. Gei and K. C. Mutasa. "Optimisation of hierarchical dielectric elastomer laminated composites". In: *International Journal of Non-Linear Mechanics* 106 (2018), pp. 266–273. DOI: 10.1016/j.ijnonlinmec.2018.06.005.

[29] A. J. Gil and R. Ortigosa. "A new framework for large strain electromechanics based on convex multi-variable strain energies: Variational formulation and material characterisation". In: *Computer Methods in Applied Mechanics and Engineering* 302 (2016), pp. 293–328. DOI: 10.1016/j.cma.2015.11.036.

[30] S. Hartmann and P. Neff. "Polyconvexity of generalized polynomial-type hyperelastic strain energy funtions for near-incompressibility". In: *International Journal of Solids and Structures* 40 (2003), pp. 2767–2791. DOI: 10.1016/S0020-7683(03)00086-6.

[31] P. Haupt. *Continuum Mechanics and Theory of Materials*. 2nd ed. Springer Berlin Heidelberg, 2002.

[32] P. Haupt. *Viskoelastizität und Plastizität*. Springer Berlin Heidelberg, 1977.

[33] D. Haussler. "Quantifying inductive bias: AI learning algorithms and Valiant's learning framework". In: *Artificial Intelligence* 36.2 (1988), pp. 177–221. DOI: 10.1016/0004-3702(88)90002-1.

[34] H. Hencky. "Über die Form des Elastizitätsgesetzes bei ideal elastischen Stoffen". In: *Zeitschrift für technische Physik* 9 (1928), pp. 215–220.

[35] H. Hencky. "Welche Umstände bedingen die Verfestigung bei der bildsamen Verformung von festen isotropen Körpern?" In: *Zeitschrift für Physik* 55 (1929), pp. 145–155.

[36] G. A. Holzapfel. *Nonlinear Solid Mechanics: A Continuum Approach for Engineering*. 2nd ed. Wiley, 2000.

[37] K. Hornik. "Approximation capabilities of multilayer feedforward networks". In: *Neural Networks* 4.2 (1991), pp. 251–257. DOI: 10.1016/0893-6080(91)90009-T.

[38] C. Huang and Q. Zhang. "Enhanced dielectric and electromechanical responses in high dielectric constant all-polymer percolative composites." In: *Advanced Functional Materials* 14 (2004), pp. 501–506. DOI: 10.1002/adfm.200305021.

[39] C. Huang, Q. M. Zhang, G. deBotton, and K. Bhattacharya. "All-organic dielectric-percolative three-component composite materials with high electromechanical response." In: *Applied Physics Letters* 84 (2004), pp. 4391–4393. DOI: 10.1063/1.1757632.

[40] E. Hüllermeier and W. Waegeman. "Aleatoric and epistemic uncertainty in machine learning: An introduction to concepts and methods". In: *Machine Learning* 110 (2021), pp. 457–506. DOI: 10.1007/s10994-021-05946-3.

[41] M. Itskov. *Tensor Algebra and Tensor Analysis for Engineers*. 5th ed. Springer Cham, 2019. DOI: 10.1007/978-3-319-98806-1.

[42]   M. Jamshidian, N. Boddeti, D. Rosen, and O. Weeger. "Multiscale modelling of soft lattice metamaterials: Micromechanical nonlinear buckling analysis, experimental verification, and macroscale constitutive behaviour". In: *International Journal of Mechanical Sciences* 188 (2020), p. 105956. DOI: `10.1016/j.ijmecsci.2020.105956`.

[43]   K. A. Kalina, L. Linden, J. Brummund, P. Metsch, and M. Kästner. "Automated constitutive modeling of isotropic hyperelasticity based on artificial neural networks". In: *Computational Mechanics* 69 (2022), pp. 1–20. DOI: `10.1007/s00466-021-02090-6`.

[44]   G. Karniadakis, I. Kevrekidis, L. Lu, P. Perdikaris, S. Wang, and L. Yang. "Physics-informed machine learning". In: *Nature Reviews Physics* (2021). DOI: `10.1038/s42254-021-00314-5`.

[45]   M. Keip, P. Steinmann, and Schröder. "Two-scale computational homogenization of electro-elasticity at finite strains". In: *Computer Methods in Applied Mechanics and Engineering* 278 (2014), pp. 62–79. DOI: `10.1016/j.cma.2014.04.020`.

[46]   T. Kirchdoerfer and M. Ortiz. "Data-driven computational mechanics". In: *Computer Methods in Applied Mechanics and Engineering* 304 (2016), pp. 81–101. DOI: `10.1016/j.cma.2016.02.001`.

[47]   D. K. Klein, M. Fernández, R. J. Martin, P. Neff, and O. Weeger. "Polyconvex anisotropic hyperelasticity with neural networks". In: *Journal of the Mechanics and Physics of Solids* 159 (2022), p. 104703. DOI: `10.1016/j.jmps.2021.104703`.

[48]   G. Kofod, P. Sommer-Larsen, R. Kornbluh, and R. Pelrine. "Actuation response of polyacrylate dielectric elastomers". In: *Journal of Intelligent Material Systems and Structures* 14.12 (2003), pp. 787–793. DOI: `10.1177/104538903039260`.

[49]   S. Kollmannsberger, D. D'Angella, M. Jokeit, and L. Herrmann. *Deep Learning in Computational Mechanics*. Vol. 977. Studies in Computational Intelligence. Springer, 2021. DOI: `10.1007/978-3-030-76587-3`.

[50]   M. Kružík and T. Roubíček. *Mathematical Methods in Continuum Mechanics of Solids*. 1st ed. Springer International Publishing, 2019.

[51]   S. Kumar and D. M. Kochmann. "What machine learning can do for computational solid mechanics". In: *Current Trends and Open Problems in Computational Mechanics*. Ed. by F. Aldakheel, B. Hudobivnik, M. Soleimani, H. Wessels, C. Weißenfels, and M. Marino. Cham: Springer International Publishing, 2022, pp. 275–285. DOI: `10.1007/978-3-030-87312-7_27`.

[52]   O. Kunc and F. Fritzen. "Finite strain homogenization using a reduced basis and efficient sampling". In: *Mathematical and Computational Applications* 24.2 (2019), p. 56. DOI: `10.3390/mca24020056`.

[53]   P. Le Tallec. "Numerical methods for nonlinear three-dimensional elasticity". In: vol. 3. Handbook of Numerical Analysis. Elsevier, 1994, pp. 465–622. DOI: `10.1016/S1570-8659(05)80018-3`.

[54]   T. Li, C. Keplinger, R. Baumgartner, S. Bauer, W. Yang, and Z. Suo. "Giant voltage-induced deformation in dielectric elastomers near the verge of snap-through instability". In: *Journal of the Mechanics and Physics of Solids* 61.2 (2013), pp. 611–628. DOI: `10.1016/j.jmps.2012.09.006`.

[55]   J. Ling, R. Jones, and J. Templeton. "Machine learning strategies for systems with invariance properties". In: *Journal of Computational Physics* 318 (2016). DOI: `10.1016/j.jcp.2016.05.003`.

[56]   K. Linka, M. Hillgärtner, K. Abdolazizi, R. Aydin, M. Itskov, and C. Cyron. "Constitutive artificial neural networks: A fast and general approach to predictive data-driven constitutive modeling by deep learning". In: *Journal of Computational Physics* (2020), p. 110010. DOI: `10.1016/j.jcp.2020.110010`.

[57]   Z. Liu, Y. Du, Y. Chen, and M. Tegmark. "Physics-augmented learning: A new paradigm beyond physics-informed learning". In: *NeurIPS 2021 AI for Science Workshop*. 2021. arXiv: `2109.13901`.

[58]   J. E. Marsden and T. J. R. Hughes. *Mathematical Foundations of Elasticity*. Ed. by D. Civil and M. Engineering. 1994.

[59]   F. Marín, J. Martínez-Frutos, R. Ortigosa, and A. J. Gil. "A convex multi-variable based computational framework for multilayered electro-active polymers". In: *Computer Methods in Applied Mechanics and Engineering* 374 (2021), p. 113567. DOI: `10.1016/j.cma.2020.113567`.

[60]   F. Masi, I. Stefanou, P. Vannucci, and V. Maffi-Berthier. "Thermodynamics-based artificial neural networks for constitutive modeling". In: *Journal of the Mechanics and Physics of Solids* 147 (2021), p. 104277. DOI: `10.1016/j.jmps.2020.104277`.

[61]   R. M. McMeeking and C. M. Landis. "Electrostatic forces and stored energy for deformable dielectric materials". In: *Journal of Applied Mechanics* 72.4 (2008), pp. 581–590. DOI: `10.1115/1.2966272`.

[62] C. Miehe, D. Vallicotti, and S. Teichtmeister. "Homogenization and multiscale stability analysis in finite magneto-electro-elasticity. Application to soft matter EE, ME and MEE composites". In: *Computer Methods in Applied Mechanics and Engineering* 300 (2016), pp. 294–346. DOI: `10.1016/j.cma.2015.10.013`.

[63] B. Moseley, A. Markham, and T. Nissen-Meyer. "Solving the wave equation with physics-informed deep learning". In: *Pre-print under review* (2020). arXiv: `2006.11894`.

[64] P. Neff, B. Eidel, and R. J. Martin. "Geometry of logarithmic strain measures in solid mechanics". In: *Archive for Rational Mechanics and Analysis* 222 (2016), pp. 507–572. DOI: `10.1007/s00205-016-1007-x`.

[65] P. Neff, K. Graban, E. Schweickert, and R. J. Martin. "The axiomatic introduction of arbitrary strain tensors by Hans Richter – A commented translation of 'Strain tensor, strain deviator and stress tensor for finite deformations'". In: *Mathematics and Mechanics of Solids* 25.5 (2020), pp. 1060–1080. arXiv: `1909.05998`.

[66] R. W. Ogden, G. Saccomandi, and I. Sgura. "Fitting hyperelastic models to experimental data". In: *Computational Mechanics* 34.6 (2004), pp. 484–502. DOI: `10.1007/s00466-004-0593-y`.

[67] A. O'Halloran, F. O'Malley, and P. McHugh. "A review on dielectric elastomer actuators, technology, applications, and challenges". In: *Journal of Applied Physics* 104.7 (2008), p. 071101. DOI: `10.1063/1.2981642`.

[68] R. Ortigosa and A. J. Gil. "A new framework for large strain electromechanics based on convex multi-variable strain energies: Finite Element discretisation and computational implementation". In: *Computer Methods in Applied Mechanics and Engineering* 302 (2016), pp. 329–360. DOI: `https://doi.org/10.1016/j.cma.2015.12.007`.

[69] R. Ortigosa, A. J. Gil, and C. H. Lee. "A computational framework for large strain nearly and truly incompressible electromechanics based on convex multi-variable strain energies". In: *Computer Methods in Applied Mechanics and Engineering* 310 (2016), pp. 297–334. DOI: `10.1016/j.cma.2016.06.025`.

[70] R. Ortigosa and J. Martínez-Frutos. "Multi-resolution methods for the topology optimization of nonlinear electro-active polymers at large strains". In: *Computational Mechanics* 68 (2021), 271–293. DOI: `10.1007/s00466-021-02030-4`.

[71] R. Pelrine, R. Kornbluh, and J. Joseph. "Electrostriction of polymer dielectrics with compliant electrodes as a means of actuation". In: *Sensors and Actuators A: Physical* 64.1 (1998), pp. 77–85. DOI: `10.1016/S0924-4247(97)01657-9`.

[72] R. Pelrine, R. Kornbluh, Q. Pei, and J. Joseph. "High-speed electrically actuated elastomers with strain greater than 100 %". In: *Science* 287.5454 (2000), pp. 836–839. DOI: `10.1126/science.287.5454.836`.

[73] R. Pelrine, R. Kornbluh, Q. Pei, S. Stanford, S. Oh, J. Eckerle, R. J. Full, M. A. Rosenthal, and K. Meijer. "Dielectric elastomer artificial muscle actuators: Toward biomimetic motion". In: *Smart Structures and Materials 2002: Electroactive Polymer Actuators and Devices (EAPAD)*. Vol. 4695. International Society for Optics and Photonics. SPIE, 2002, pp. 126 –137. DOI: `10.1117/12.475157`.

[74] C. Sansour. "On the physical assumptions underlying the volumetric-isochoric split and the case of anisotropy". In: *European Journal of Mechanics-A/Solids* 27.1 (2008), pp. 28–39. DOI: `10.1016/j.euromechsol.2007.04.001`.

[75] J. Schröder and P. Neff. "Invariant formulation of hyperelastic transverse isotropy based on polyconvex free energy functions". In: *International Journal of Solids and Structures* 40 (2003), pp. 401–445. DOI: `10.1016/S0020-7683(02)00458-4`.

[76] J. Schröder, P. Neff, and D. Balzani. "A variational approach for materially stable anisotropic hyperelasticity". In: *International Journal of Solids and Structures* 42 (2005), pp. 4352–4371. DOI: `10.1016/j.ijsolstr.2004.11.021`.

[77] J. Schröder and P. Neff. "Invariant formulation of hyperelastic transverse isotropy based on polyconvex free energy functions". In: *International Journal of Solids and Structures* 40 (2003), pp. 401–445. DOI: `10.1016/S0020-7683(02)00458-4`.

[78] J. Schröder, P. Neff, and V. Ebbing. "Anisotropic polyconvex energies on the basis of crystallographic motivated structural tensors". In: *Journal of the Mechanics and Physics of Solids* 56 (2008), pp. 3486–3506. DOI: `10.1016/j.jmps.2008.08.008`.

[79] B. Shrimali, V. Lefevre, and O. Lopez-Pamies. "A simple explicit homogenization solution for the macroscopic elastic response of isotropic porous elastomers". In: *Journal of the Mechanics and Physics of Solids* 122 (2019), pp. 364–380. DOI: `10.1016/j.jmps.2018.09.026`.

[80] M. H. Siboni, R. Avazmohammadi, and P. P. Castañeda. "Electromechanical instabilities in fiber-constrained, dielectric-elastomer composites subjected to all-around dead-loading". In: *Mathematics and Mechanics of Solids* (2014). DOI: 10.1177/1081286514551501.

[81] M. H. Siboni and P. P. Castañeda. "Fiber-constrained, dielectric-elastomer composites: Finite-strain response and stability analysis". In: *Journal of the Mechanics and Physics of Solids* 68.0 (2014), pp. 211–238. DOI: 10.1016/j.jmps.2014.03.008.

[82] M. Silhavy. "A variational approach to nonlinear electro-magneto-elasticity: Convexity conditions and existence theorems". In: *Mathematics and Mechanics of Solids* 23.6 (2018), pp. 907–928. DOI: 10.1177/1081286517696536.

[83] M. Silhavy. *The Mechanics and Thermodynamics of Continuous Media*. 1st ed. Theoretical and Mathematical Physics. Springer Berlin Heidelberg, 2014.

[84] A. L. Skov, O. Pei, D. Opris, R. J. Spontak, G. Gallone, H. Shea, and M. Y. Benslimane. "Dielectric elastomers (DEs) as EAPs: Materials". In: *Electromechanically Active Polymers: A Concise Reference*. Cham: Springer International Publishing, 2016, pp. 1–28. DOI: 10.1007/978-3-319-31767-0_31-1.

[85] P. Steinmann, M. Hossain, and G. Possart. "Hyperelastic models for rubber-like materials: Consistent tangent operators and suitability for Treloar's data". In: *Archive of Applied Mechanics* 82 (2012), pp. 1183–1217. DOI: 10.1007/s00419-012-0610-z.

[86] V. Tac, F. S. Costabal, and A. B. Tepole. "Automatically polyconvex strain energy functions using neural ordinary differential equations". In: *Pre-print under review* (2021). arXiv: 2110.03774.

[87] V. Tac, V. D. Sree, M. K. Rausch, and A. B. Tepole. "Data-driven modeling of the mechanical behavior of anisotropic soft biological tissue". In: *Pre-print under review* (2021). arXiv: 2107.05388.

[88] P. Thakolkaran, A. Joshi, Y. Zheng, M. Flaschel, L. De Lorenzis, and S. Kumar. "NN-EUCLID: Deep-learning hyperelasticity without stress data". In: *Pre-print under review* (2022). arXiv: 2205.06664.

[89] L. Treloar. *The Physics of Rubber Elasticity*. Oxford Classic Texts in the Physical Sciences. Oxford University Press, USA, 1975.

[90] C. Truesdell and W. Noll. *The Non-Linear Field Theories of Mechanics*. 3rd ed. Springer Berlin Heidelberg, 2004.

[91] N. N. Vlassis, R. Ma, and W. Sun. "Geometric deep learning for computational mechanics part I: Anisotropic hyperelasticity". In: *Computer Methods in Applied Mechanics and Engineering* 371 (2020). DOI: 10.1016/j.cma.2020.113299.

[92] N. N. Vlassis and W. Sun. "Sobolev training of thermodynamic-informed neural networks for interpretable elasto-plasticity models with level set hardening". In: *Computer Methods in Applied Mechanics and Engineering* 377 (2021), p. 113695. DOI: 10.1016/j.cma.2021.113695.

[93] D. K. Vu and P. Steinmann. "On the spatial and material motion problems in nonlinear electro-elastostatics with consideration of free space". In: *Mathematics and Mechanics of Solids* 17 (2012), pp. 803–823. DOI: 10.1177/1081286511430161.

[94] D. K. Vu, P. Steinmann, and G. Possart. "Numerical modelling of non-linear electroelasticity". In: *International Journal for Numerical Methods in Engineering* 70.6 (2007), pp. 685–704. DOI: 10.1002/nme.1902.

[95] P. Weber, J. Geiger, and W. Wagner. "Constrained neural network training and its application to hyperelastic material modeling". In: *Computational Mechanics* 68 (2021), 1179–1204. DOI: 10.1007/s00466-021-02064-8.

[96] P. Wriggers. *Nonlinear Finite Element Methods*. 1st ed. Springer Berlin Heidelberg, 2008. DOI: 10.1007/978-3-540-71001-1.

[97] L. Zee and E. R. Sternberg. "Ordinary and strong ellipticity in the equilibrium theory of incompressible hyperelastic solids". In: *Archive for Rational Mechanics and Analysis* 83 (1983), pp. 53–90. DOI: 10.1007/BF00281087.

[98] Q.-S. Zheng. "Theory of representations for tensor functions — A unified invariant approach to constitutive equations". In: *Applied Mechanics Reviews* 47.11 (1994), pp. 545–587. DOI: 10.1115/1.3111066.

[99] Q.-S. Zheng and A. Spencer. "Tensors which characterize anisotropies". In: *International Journal of Engineering Science* 31.5 (1993), pp. 679 –693. DOI: 10.1016/0020-7225(93)90118-E.

[100] Q.-S. Zheng and A. Spencer. "On the canonical representations for Kronecker powers of orthogonal tensors with application to material symmetry problems". In: *International Journal of Engineering Science* 31.4 (1993), pp. 617 –635. DOI: 10.1016/0020-7225(93)90054-X.